Seismic investigation of an active ocean-continent transform margin: the interaction between the Swan Islands Fault Zone and the ultraslow-spreading Mid-Cayman Spreading Centre

C. Peirce[1], A.H. Robinson[1], A.M. Campbell[1], M.J. Funnell[1], I. Grevemeyer[2], N.W. Hayman[3], H.J.A. Van Avendonk[3] & G. Castiello[1],

[1] Department of Earth Sciences, Durham University, South Road, Durham, DH1 3LE, UK.

[2] GEOMAR Helmholtz Centre for Ocean Research, Kiel, Germany.

[3] Institute for Geophysics, Jackson School of Geosciences, University of Texas, Austin, Texas, USA.

Accepted Received in original form

Abbreviated title: Transform ocean-continent boundaries – the Swan Islands margin

Corresponding author:

Christine Peirce
Department of Earth Sciences
Durham University
South Road
Durham
DH1 3LE
United Kingdom
Email: christine.peirce@durham.ac.uk

SUMMARY

The Swan Islands Transform Fault (SITF) marks the southern boundary of the Cayman Trough and the ocean-continent transition of the North American-Caribbean plate boundary offshore Honduras. The *CAYSEIS* experiment acquired a 180 km-long seismic refraction and gravity profile across this transform margin, ~70 km to the west of the Mid-Cayman Spreading Centre (MCSC). This profile shows the crustal structure across a transform fault system that juxtaposes Mesozoic-age continental crust to the south against the ~10 Ma-old ultraslow spread oceanic crust to the north.

Ocean-bottom seismographs were deployed along-profile, and inverse and forward travel-time modelling, supported by gravity analysis, reveals ~23 km-thick continental crust that has been thinned over a distance of ~70 km to ~10 km at the SITF, juxtaposed against ~4 km-thick oceanic crust. This thinning is primarily accommodated within the lower crust. Since Moho reflections are not widely observed, the 7.0 km s^{-1} velocity contour is used to define the Moho along-profile. The apparent lack of reflections to the north of the SITF suggests that the Moho is more likely a transition zone between crust and mantle.

Where the profile traverses bathymetric highs in the off-axis oceanic crust, higher P-wave velocity is observed at shallow crustal depths. S-wave arrival modelling also reveals elevated velocities at shallow depths, except for crust adjacent to the SITF that would have occupied the inside corner high of the ridge-transform intersection when on axis. We use a Vp/Vs ratio of 1.9 to mark where lithologies of the lower crust and uppermost mantle may be exhumed, and also to locate the upper-to-lower crustal transition, identify relict oceanic core complexes and regions of magmatically formed crust. An elevated Vp/Vs ratio suggests not only that serpentinized peridotite may be exposed at the seafloor in places, but also that seawater has been able to flow deep into the crust and upper mantle over 20-30 km-wide regions which may explain the lack of a distinct Moho.

The SITF has higher velocities at shallower depths than observed in the oceanic crust to the north and, at the seabed, it is a relatively wide feature. However, the velocity-depth model sub-seabed suggests a fault zone no wider than ~5-10 km, that is mirrored by a narrow seabed depression ~7500 m-deep. Gravity modelling shows that the SITF is also underlain, at >2 km sub-seabed, by a ~20 km-wide region of density >3000 kg m^{-3} that may reflect a broad region of metamorphism. The residual mantle Bouguer anomaly across the survey region, when compared with the bathymetry, suggests that the transform may also have a component of left-lateral trans-tensional displacement that accounts for its apparently broad seabed appearance, and that the focus of magma supply may currently be displaced to the north of the MCSC segment centre.

Our results suggest that Swan Islands margin development caused thinning of the adjacent continental crust, and that the adjacent oceanic crust formed in a cool ridge setting, either as a result of reduced mantle upwelling and/or due to fracture enhanced fluid flow.

Key words: continental margins: transform, controlled source seismology, crustal structure, oceanic transform and fracture zone processes.

1. INTRODUCTION

Passive rifted margins are segmented in many places by large-scale lateral transform faults and fracture zones. Despite their relative abundance, transform ocean-continental margins remain far less frequently studied and, hence, less well understood than other margins. The continental crust associated with these margins is juxtaposed against adjacent oceanic crust across fracture zones which, in turn, can be traced in the free-air gravity anomaly to a corresponding offset in the adjacent mid-ocean ridge or spreading centre.

In addition to their accompanying fracture zones, within localized ocean-continent transitions (OCT – Sage et al., 2000) transform margins also exhibit characteristically steep continental slopes adjacent to an elevated basement surface known as a marginal ridge (Francheteau and Le Pichon, 1972; Mascle, 1976). Heat flow between adjacent old cold continental and young hot oceanic lithosphere (Todd et al., 1988; Lorenzo and Vera, 1992; Gadd and Scrutton, 1997), or compressional tectonics (Blarez and Mascle, 1988) and rapid variation in subsidence and/or magmatic underplating (Basile et al., 1998), are all processes used to explain the origin of these pronounced bathymetric ridges. Ocean-continent transforms are also hypothesized to initiate by ridge jumps after rifting (e.g. Taylor et al., 2009), since they can accommodate very large offsets that ultimately lead to large-scale plate reorganizations (Dalziel and Dewey, 2018). However, little is known about their active stages of development with key questions being:

1) can an ocean-continent transform develop without stretching of the adjacent continental crust? and
2) is the mid-ocean ridge and oceanic crust near the intersection with an OCT different due to reduced mantle upwelling?

Most conceptual models envision that transform margins evolve through a series of stages (e.g. Le Pichon and Hayes, 1971; Scrutton, 1979; Mascle and Blarez, 1987; Mascle et al., 1997; Peirce et al., 1996; Greenroyd et al., 2007, 2008 – Fig. 1):

Stage 1: rifting - initial intracontinental rifting consists of many small faults. As rifting progresses, these faults link together to form larger-scale rift- and transform-style structures. As rifting continues the continental crust thins orthogonal to the rift axis and several distinct rift segments form, each separated by a transform.

Stage 2: drifting - crustal thinning proceeds to such an extent that plate separation finally occurs and oceanic spreading centres form, and spreading results in the juxtaposition of old continental lithosphere against young oceanic lithosphere across a transform and the continental plates continue to drift apart.

Stage 3: aging - eventually transform motion ceases and the margin becomes inactive, and thinned continental crust may ultimately become juxtaposed against, and coupled to, normal thickness oceanic crust across a fracture zone.

However, the degree to which the oceanic and continental lithosphere are mechanically and thermally coupled throughout these stages of breakup is not well understood, and neither are their thermal history and strength profile. Furthermore, transform faults are thought to be sites of significant mantle hydration (White et al., 1984). As serpentinite can weaken faults, allowing for large-scale slip (Escartín et al., 1997), it may play a friction-reducing role between the two plates during the drifting stage, further facilitating structural segmentation.

The deep structure of transform margins has been modelled with both gravity and wide-angle seismic refraction data, suggesting that the continental crust thins sharply over a distance of less than 10-40 km. For example, the Ghana (Edwards et al., 1997) and French Guiana (Greenroyd et al., 2008) margins exhibit continental crustal thinning over zones 10-20 km and ~40 km-wide respectively. Edwards et al. (1997) also note the presence of a zone of high density (3100 kg m^{-3}), high velocity (5.8-7.3 km s^{-1}) and high magnetization (1.10-1.25 A m^{-1}) at the ocean-continent boundary of the Ghana transform margin, which they suggest may be a consequence of either intrusion by basic igneous rocks or serpentinization of the upper mantle. However, a recent compilation by Mercier de Lepinay et al. (2016) suggests that transform margins may have a diverse range of characteristics, including:

i) a continental slope steeper on average than passive margins, although some transform margin slopes are quite similar to passive margins;
ii) a 50 to 100 km-wide zone of continental crustal thinning that is significantly narrower than at passive margins, suggesting deformation is focused in a sub-vertical fault;
iii) a marginal ridge parallel to the OCT that is observed only at a few transform margins; and
iv) a marginal plateau - a deep and flat surface within the continental slope interpreted as a thin continental crust domain inherited from a stretching event older than the formation of the transform margin itself.

However, the majority of the studies conducted to date are focused on fossil transform margins (Stage 3), where active lateral motion has ceased and where the margin is covered by a thick layer of sediments, placing the igneous basement several kilometres below the current seafloor (e.g. Christeson, et al., 2010).

Detrick et al.'s (1993) review of seismic studies at the slow-spreading Mid-Atlantic Ridge concludes that large-offset transform faults exhibit anomalous crustal structures being extremely heterogeneous in both thickness and internal structure. The crust around these faults can be quite thin (<1-2 km-thick) and characterized by low P-wave velocities and an absence of a normal oceanic layer 3. The geological interpretation of the limited extant seismic observations (e.g. White et al., 1984; Müller et al., 2000; Kuna et al., 2019; Peirce et al., 2019) is that the crust within transform faults consists of a thin, intensely fractured, and hydrothermally altered basaltic section overlying ultramafic rocks that are extensively serpentinized. The existence of a thin crustal section can be explained by a reduced magma supply at the mid-ocean ridge-transform intersection (Tolstoy et al., 1993). In the case of an ultraslow-spreading centre, the magma supply at the segment ends, in the vicinity of the offsetting transform fault, may be even lower and result in even thinner crust given seismic thickness estimates for ultraslow crust worldwide (e.g. White et al., 1984).

In this paper, we present the results of a multi-disciplinary geophysical investigation of an ocean-continent transform margin that is currently actively evolving. Wide-angle seismic and gravity data have been analysed and modelled using both inversion and forward approaches. The resulting models, together with the seabed morphology, reveal the structure of the ocean-continent transition, the nature of the transform fault, the characteristics of the young oceanic crust produced at the adjacent spreading centre, and the relationship between the two. We also investigate if an ocean-continent transform margin can develop without stretching of the adjacent crust, and if that crust acts as a heat sink cooling the adjacent ridge axis, impacting on magma dynamics and flow along-axis.

2. STUDY LOCATION AND GEOLOGICAL SETTING

The Swan Islands transform margin, located in the Caribbean Sea at the southern edge of the Cayman Trough (Fig. 2), is marked by the Swan Islands Transform Fault (SITF). This margin is currently actively evolving (Mercier de Lepinay et al., 2016) and is one of few identified to be in Stage 2; the Gulf of California is another example. Using gravity and magnetic data, ten Brink et al. (2002) presented models of Cayman Trough formation where 2-3 km-thick, zero-age to 45 My-old oceanic crust is juxtaposed against 20-30 km-thick continental crust adjacent to the ultraslow spreading Mid-Cayman Spreading Centre (MCSC – full rate of 15-17 mm y^{-1} – Holcombe and Sharman, 1973; Dick et al., 2003; DeMets et al., 2007). Consequently, at their intersection young hot oceanic lithosphere is juxtaposed against old cold continental lithosphere, making this an ideal location not only to study how these margins evolve, but to also investigate if the adjacent continental crust becomes thinned and the adjacent ridge axis cooled as part of that formation process.

2.1. Swan Islands Transform Fault boundary

In the late Cretaceous, a sinistral (~20 mm y^{-1} left lateral – Rosencrantz and Mann, 1991; Hayman et al., 2011; Graham et al, 2012) strike-slip zone developed between the Caribbean plate and the Yucatan Block, offsetting the "Great Arc of the Caribbean" (Mann, 2007). The MCSC formed within this shear zone in the Eocene (~49 Ma) (Rosencrantz and Mann, 1991; Leroy et al., 2000). At ~20 Ma, the Chortis (continental) Block was transported along the Motagua Fault (Rogers et al., 2007b; Boschman et al., 2014; Sanchez et al., 2016). At the present time, the Chortis Block lies to the south of the active MCSC and the SITF marks the boundary between it and the Mayan Block on the continental side of the OCT (Rogers et al., 2007a).

The SITF is, thus, part of a very large strike-slip system that includes the Motagua Fault (Honduras) and the Enriquillo-Plantain Garden Fault Zone (Fig. 2a), along which the 2010 Haiti earthquake occurred (Mercier de Lepinay et al., 2011). That moment magnitude (M_w) 7.0 earthquake initiated along a fault system that connects the Puerto Rico Trench and the SITF, part of which marks the northernmost boundary of the Caribbean plate (Fig. 2b). The Swan Island Transform Fault itself has generated two of the largest earthquake events in the Caribbean Sea - a M_w 7.3 earthquake in 2009, and a M_w 7.6 earthquake in January 2018 (Fig. 2 – USGS Earthquake Hazards Program catalogue; https://earthquake.usgs.gov). Motion along these major strike slip faults is linked with seafloor spreading at the MCSC in the Cayman Trough.

Little is known specifically about the crustal structure of the SITF apart from that revealed by a seismic reflection profile located across the northern Honduras margin. In that study, Sanchez et al. (2016) define the margin as an active transform margin separating the Caribbean and North American plates, in which a 120 km-wide Honduran borderland adjacent to the Cayman Trough is characterized by narrow rift basins with normal faulting running margin-parallel. Sanchez et al. (2016) attribute the observed crustal thinning to a phase of Oligocene-Recent trans-tension.

Rosencrantz and Mann (1991) describe the tectonic structure of the seabed within the Swan Islands and Walton Transform Faults (Fig. 2b) using swath bathymetry data acquired by SeaMARC II, with the SITF dominated by two major strands that overlap ~70 km west of the Swan Islands. The western lineament runs at an azimuth of 070° for 275 km from the southwest corner of the Cayman Trough as the seaward continuation of the

onshore Motagua Fault, while the eastern lineament extends for 320 km towards the southern end of the MCSC, passing south of the Swan Islands at 077° along a more sinuous trend than in the west. At its eastern end, a shorter lineament, located 5 km to the north, curves north-eastwards towards and into the MCSC axial rift zone. Consequently, adjacent to the MCSC the SITF is perhaps more appropriately termed the Swan Islands Transform Fault Zone.

Based on satellite gravity data, ten Brink et al. (2002) proposed a model of the SITF which suggests that the oceanic crust for 50 km on either side of the spreading centre is only 2-3 km thick and juxtaposed against 20-30 km-thick continental crust to the south. However, the gravity data lack sufficient resolution to confidently constrain crustal thickness as do seismic refraction measurements made by Ewing et al. (1960).

2.2. MCSC

The MCSC lies at the centre of the Cayman Trough. It is the deepest known seafloor spreading centre, ranging in depth from ~4200 m to >6000 m, and magnetic anomalies indicate ultraslow seafloor spreading has been on-going for the past 45.6 My (Rosencrantz et al., 1988; Leroy et al., 2000). The northern end of the MCSC hosts the world's deepest known black smoker system (German et al., 2009; Connelly et al., 2012) including an off-axis, moderate-temperature sulphide vent known as the Von Damm field. Swath bathymetry data reveals oceanic core complexes (OCCs) on-axis, with the central one, Mt Dent, hosting the Von Damm field in an exhumed mafic crustal root (Connelly et al., 2012; Harding et al., 2017; Van Avendonk et al., 2017; Grevemeyer et al., 2018a).

Observation of OCCs and their corrugated detachment surfaces, exposing gabbro and peridotite lithologies at the seabed in between basalts (Stroup and Fox, 1981; Hayman et al, 2011; Haughton et al., 2019), suggests that the crust has formed as a result of phases of tectonic and magmatic seafloor spreading (e.g. Olive et al., 2010). Searle (2012) conclude that along-axis variations in volcanism and tectonism might reflect an underlying, highly laterally variable crustal structure, including variation in crustal thickness. In fact, existing geophysical data suggest the Cayman Trough contains some of the thinnest (~3 km) oceanic crust on Earth (Ewing et al., 1960; White at al., 2001; ten Brink et al., 2002; Harding et al., 2017; Van Avendonk et al., 2017; Grevemeyer et al., 2018a). Grevemeyer et al. (2018a) subsequently hypothesize that older portions of the Cayman Trough correlate with predominantly magma-poor seafloor spreading.

The oceanic lithosphere within the Cayman Trough is quite heterogeneous, although overall a melt-poor system. The nature of the ocean-continent transition between the Cayman Trough and adjacent continental blocks is similarly remarkable for anomalously deep bathymetry adjacent to steep seabed gradients. Although no seafloor sampling of the geology of the SITF has been conducted, dredging on the adjacent Walton Transform Fault system to the east has recovered serpentinized peridotite (Hayman et al., 2011). Elsewhere magma-poor ocean-continent transitions are associated with significant crustal stretching (e.g. Lavier and Manatschal, 2006). Consequently, at the Swam Islands margin not only can a transform margin that is actively evolving be studied, but also one that is acting, in many respects, as a magma-starved ocean-continent transition.

3. DATA ACQUISITION

In April 2015, during the FS Meteor cruise M115 (Grevemeyer et al., 2016; Peirce, 2015), a multi-national project (*CAYSEIS - Crustal accretion and transform margin evolution at ultraslow spreading rates*) acquired active-source seismic, gravity, magnetic and swath bathymetry data along six profiles (called Profiles P01-P06) in the Cayman Trough (Fig. 3), together with passive seismic data surrounding the Mt Dent OCC. Here we describe one of these profiles (Profile P04) located ~70 km to the west of the MCSC spreading axis (Fig. 3), running ridge-axis-parallel and traversing the SITF and crossing the Swan Island transform ocean-continental margin. Profile P04 runs approximately parallel to the seafloor-spreading isochrons, through crust that could range from 10 to 12 My in age depending on spreading rate. The exact spreading rate is difficult to determine with any precision as magnetic anomalies are poorly defined (Hayman et al., 2011). The profile is located in the region of negative magnetic polarity just west of anomaly 5 and, therefore, older than ~10 Ma but younger than 12 Ma (Leroy et al., 2000). Here we assume a half spreading rate of 7.5 mm y^{-1} and, for simplicity, refer to the crustal age along Profile P04 as ~10 Ma. Profiles acquired along and across the MCSC are described by Harding et al. (2017 – Profile P02), Van Avendonk et al. (2017 – Profile P01) and Grevemeyer et al. (2018a – Profiles P05 and P06).

Along Profile P04, wide-angle (WA) seismic data were acquired with 36 ocean-bottom seismographs (OBSs) and hydrophones (OBHs) spaced at ~5 km intervals along a total profile length of ~180 km (Fig. 3). Each OBS had a three-component geophone and a hydrophone, while each OBH was fitted with a hydrophone only (see Acknowledgements for instrument sources). Henceforth, we refer to both instrument types as OBSs for simplicity. Data were recorded at 4 ms (250 Hz) sampling rate.

All the OBSs recorded excellent quality data, except OBSs 419 and 422 which failed to record any data or had unresolvable timing issues. Water waves and first-arriving refracted phases (crustal Pg and mantle Pn) are observed for all shots, together with variable unequivocal observations of Moho reflections (PmP) and second-arriving S-waves (Sg); the latter primarily for oceanic crustal regions and the former for continental regions.

Shots were fired using an array of 12 Sercel G airguns of 260, 380 and 520 in^3 chamber sizes, arranged in two identical sub-arrays of six guns, towed at 7.5 m depth. The total array volume was 5440 in^3 (~89 l), which was fired at 60 s intervals at an air pressure of 3000 psi (~207 bar). This firing interval at 4.5 kn surveying speed resulted in a shot interval of ~150 m, for a total of 1169 shots.

Gravity data were acquired port-to-port (see Fig. 2a for the cruise track) using a LaCoste-Romberg/Micro-G air-sea gravimeter mounted on a gyro-stabilized platform. The meter was provided with a GPS navigation stream and tied to absolute base stations in Montego Bay (Jamaica) and Pointe-a-Pitre (Guadeloupe), the cruise port calls. Data were reduced to the free-air anomaly (FAA) for modelling. Swath bathymetry data were acquired along profiles using a Kongsberg Simrad EM122 multi-beam echo-sounder, calibrated with a sound velocity profile conducted in the survey area to full ocean depth. These profiles were quality control edited before merging with existing data and gridding at 150 m node intervals.

4. WIDE-ANGLE DATA TRAVEL-TIME PICKING

The variation in seabed depth and sediment cover control the signal-to-noise ratio (SNR) and phase recording characteristics of each OBS dataset. Prior to travel-time picking, phase types were identified as water wave direct

arrivals (Ww) and their sea-surface/seabed multiples, crustal refracted arrivals (Pg and Sg) and mantle refracted arrivals (Pn) by analysis of the OBS data displayed at a range of reduction velocities. Example record sections for OBSs 410, 420 and 430 are shown in Fig. 4, chosen to represent the three different geological settings: oceanic crust (OBS 410), OCT (OBS 420) and continental crust (OBS 430).

4.1. Oceanic crust: OBS 410

OBS 410 (Fig. 4a,b) is located on ~10 My-old oceanic crust ~60 km to the north of the SITF, and shows clear evidence for both P-wave and S-wave refractions. PmP reflections from the Moho are not unequivocally observed on any OBS located to the north of the SITF, which suggests that the Moho here may not be a distinct interface at the wavelength of the seismic signal generated by the G airgun array and, instead, it is effectively a transition zone. Crustal Pg arrivals are observed at the nearest shot-receiver offsets as there is little-to-no sediment cover. Pn arrivals are generally observed at offsets >35 km from the instrument. Pg apparent velocities vary from 3.5 to 6.8 km s^{-1} for offsets sampling the upper crust, while apparent velocities range between 6.8 and 7.0 km s^{-1} for the lower crust. Pn arrivals range in apparent velocity between 7.1 and 8.0 km s^{-1} (Fig. 4a,b). Undulation in first-arrival travel times is largely a function of variation in seabed topography along profile.

4.2. OCT: OBS 420

OBS 420 (Fig. 4c,d) is located at the SITF, the topographically most variable area along the profile. Although clear Pg and Pn arrivals are observed, S-waves (i.e. for the entire sub-seabed propagation path) are quite limited. The general lack of S-wave arrivals suggests that the internal structure of the transform zone acts as a vertical barrier to lateral propagation. Pg arrivals can be observed from the shortest offsets which suggests that a significant thickness of sediment originating, for example, from the adjacent continental margin, has not accumulated within the SITF. Pn arrivals are evident at offsets greater than 40 km from the instrument. Pg arrivals are characterized by apparent velocities between 4.8 and 6.8 km s^{-1} for offsets sampling the upper crust, and between 6.9 and 7.0 km s^{-1} for the lower crust. Pn arrivals range in apparent velocity between 7.3 and 8 km s^{-1} (Fig. 4c,d).

4.3. Continental crust: OBS 430

OBS 430 (Fig. 4e,f) is located on the continental slope towards the southern end of the profile. The shallowing seabed depth to the south of this instrument results in the observed record section asymmetry. Crustal and mantle refracted arrivals are clearly visible on the record section, together with a set of slower apparent velocity arrivals over a distance of <3 km either side of the instrument location. These arrivals could suggest a relatively thin veneer of sediment cover and may explain the better SNR of instruments to the south of the SITF, due to the better seabed sensor coupling and less signal scattering as a result. Pn arrivals are observed at shot-receiver offsets of >50 km. Considering both upper and lower crust arrivals together, Pg apparent velocities range between 2.2 and 7.0 km s^{-1}, and Pn arrivals range between 7.4 and 8 km s^{-1} (Fig. 4e,f), which may reflect an apparent thinning of the crust and/or dip of the Moho. The only PmP arrivals unequivocally observed anywhere along Profile P04 are observed by instruments located to the south of the SITF and, even then, they are of low amplitude and sparse. Thus, PmP occurs in the continental domain rather than being a feature of oceanic crust accreted at the MCSC. Similarly, S-

waves are generally not observed to the south of the SITF, being of very limited extent on specific OBSs of which OBS 430 is an example.

5. WIDE-ANGLE DATA INVERSION MODELLING

First-arrival travel times were picked from the hydrophone record for each instrument, as this displayed the highest SNR. Pick uncertainties of 50 ms for P-waves and 100 ms for S-waves were assigned for each sub-seabed travelling phase regardless of shot-receiver offset and, thus, turning depth. These uncertainties were calculated based on instrument and shot location errors and considering the SNR for each phase type. Approximately 21,900 first-arrival travel time picks were made from 34 receiver gathers. Prior to inversion, OBS locations on the seabed along-profile were accurately determined by forward ray-trace modelling water wave arrivals (Ww) and their multiples using *rayinvr* (Zelt and Ellis 1988; Zelt and Smith 1992). The water column velocity structure was based on the sound velocity profile used to calibrate the swath bathymetry acquisition system. The model seabed interface was created by sampling the bathymetry at 0.25 km intervals along-profile, and projecting these and the OBS and shot locations into kilometre-space relative to 17° 04.744'N / 82° 17.752'W – the first shot point – prior to padding the model at either end to minimise edge effects. The inversion forward model was discretized on a 0.25 by 0.25 km uniform square mesh (the forward cell size), which remained constant throughout inversion modelling.

5.1. Inversion process

Pg and Pn first-arrival travel time picks were first inverted for P-wave crustal velocity-depth structure using the *FAST* inversion method of Zelt and Barton (1998), as it is a modeller-independent process that could also be used to test the resolution of the resulting velocity-depth model (Zelt et al. 2003; Zelt and Barton, 2008). The inversion initial starting model (henceforth referred to as the *P-wave initial model* – Fig. 5) was constructed with a 1D velocity model applied beneath a seabed interface, with a velocity of 2.5 km s^{-1} at the seafloor and 8.5 km s^{-1} at 10 km below sea level (b.s.l.) to represent a constant depth Moho starting point, approximately mid-way between that of average oceanic and continental crusts. This starting model enabled the greatest modelling freedom within existing geological constraint but, more importantly, did not impose any structure associated with the SITF or the OCT, or impose any velocity-depth expectation for the oceanic crust.

The inversion was run in two phases; first, one of five non-linear inversion iterations followed by one of eight, with the inversion cell size reduced between phases from 2.0 x 1.0 km for phase 1 to 1.0 x 0.5 km for phase 2. The model resulting from phase 1 (Fig. 5 – henceforth referred to as the *P-wave interim model*) was used as the starting model for phase 2. After phase 1 the model had a T_{RMS} misfit of ~97 ms and a χ^2 = ~3.7, improving after phase 2 to a T_{RMS} misfit of ~81 ms and χ^2 = ~2.6 for the final model (Fig. 5 – henceforth the *P-wave inversion model*).

As S-wave arrivals were only primarily observed to the north of the SITF, S-wave crustal velocity-depth modelling (Fig. 6) concentrated solely on the oceanic crust. The resulting model also provides a means to determine the Vp/Vs ratio which could then be used to characterize the lithology and the spreading regime in which the oceanic crust formed, using an approach similar to that described by Grevemeyer et al. (2018a). Consequently, the ~4050 Sg first-arrival travel time picks from OBSs 401-416 were then inverted for S-wave crustal velocity-

depth structure, with an initial starting model (Fig. 6a – henceforth the *S-wave initial model*) constructed with a 1D velocity model applied beneath the same seabed interface, with a velocity of 2.0 km s^{-1} at the seafloor and 5.0 km s^{-1} at 10 km b.s.l.. The inversion was again run in two phases in the same way as the P-wave inversion, but this time with the inversion cell size reduced between the phases from 3.0 x 1.0 km for phase 1 to 1.0 x 1.0 km for phase 2. After phase 1 the model (Fig. 6b – henceforth the *S-wave interim model*) had a T_{RMS} misfit of ~220 ms and a χ^2 = ~4.8, improving after phase 2 to a T_{RMS} misfit of ~166 ms and χ^2 = ~2.8 for the final model (Fig. 6c – henceforth the *S-wave inversion model*). The parameters for both P-wave and S-wave inversions are summarized in Table 1.

5.2. Model resolution testing

To test the resolution of both inversion models, checkerboard tests comprising eight iterations were performed (Fig. 7) to determine the smallest structures resolvable by the acquisition geometry and model parameterization (Zelt, 1998). A regular checkerboard of alternating polarity velocity perturbations of ±5% was convolved with both the *P-wave* and *S-wave inversion models* and synthetic travel times generated by forward ray-tracing through these models. Gaussian noise was then added based on the corresponding pick uncertainties. These synthetic travel times were inverted using the same parameters used to derive the *P-wave* and *S-wave inversion models*, with the process repeated for a broad range of checkerboard cell sizes and patterns. These patterns included lateral and vertical shifts of 0.5, 1.0 and 1.5 times the anomaly width and depth, and included patterns aligned vertically (columns) and horizontally (rows), alternating polarity of the checkerboard velocity (positive and negative), half shifts in cells (across rows and down columns) and all possible combinations thereof – 16 patterns in total. Overall, good checkerboard recovery was achieved within the crust to a depth below seabed (b.s.b.) of ~3 km for a 2 x 2 km input anomaly size for the *P-wave inversion model* (Fig. 7a,b), and a 3 x 2 km input anomaly size for the *S-wave inversion model* (Fig. 7j,k). However, below ~8 km b.s.b., the checkerboard pattern was not recovered for any applied pattern with a vertical cell size of less than 4 km, most likely due to the much sparser ray coverage below this depth.

To quantitatively assess the results from the checkerboard tests, the correlation between the applied and recovered checkerboards was calculated for each of the tested patterns (Fig. 7c,f,i,l,o & r). Zelt (1998) refers to this correlation as semblance, and defines a threshold value of 0.7 as indicating well-resolved regions of a model. The semblance calculations used the same model dimensions established for the checkerboard tests and show that the oceanic crust, together with the transform margin and lower continental slope, are well-resolved to the scale of anomaly variation necessary to determine crustal structure and any lateral variation within it.

In general terms, for an applied ±5% velocity anomaly, structures in the oceanic crust of both the *P-wave* and *S-wave inversion models* are consistently constrained with confidence to 4 km-wide by 2 km-deep to a depth of ~8 km b.s.l. for the P-wave (Fig. 7f) and 5 km-wide by 2 km-deep for the S-wave (Fig. 7o) respectively, and in the continental crust to 4 km-wide by 2 km-deep for the upper crust to a depth of ~6 km b.s.l. (Fig. 7f), and 10 km-wide by 4 km-deep for the lower crust to a depth of ~20 km b.s.l. (Fig. 7i) for areas of densest ray coverage.

5.3. Vp/Vs ratio

The *P-wave* and *S-wave inversion models* were used to calculate the Vp/Vs ratio throughout the model space to the

north of the SITF (Fig. 8f – henceforth the *Vp/Vs model*) with resulting values of <1.9 for the upper crust and >1.9 for the lower crust. Within the upper crust, a ridge-parallel lateral variation in Vp/Vs is observed which correlates with areas of shallower seabed topography. Horen et al. (1996) and Christensen (2004) found that Vp/Vs ratios >1.9 are representative of serpentines, and Grevemeyer et al. (2018a) use this marker as a discriminator between magma-rich (<1.9) and magma-poor (>1.9) crustal formation along a MCSC flow-line profile (P05 & P06 – Fig. 3). The 1.9 Vp/Vs ratio proxy also appears to hold for the ~10 Ma crust along Profile P04 off-MCSC-axis (Fig. 8f), in particular, suggesting that a region between ~115 km and ~132 km along-profile has a magma-rich origin, while the adjacent crust more likely formed by exhumation of the lower crust and uppermost mantle to upper crustal levels.

6. MODEL CONSTRAINTS

The observed free-air gravity anomaly along-profile (FAA – Fig. 9c) provides an independent test of velocity model uniqueness and gives additional constraint on poorly resolved regions. The *P-wave inversion model* was, therefore, converted into a density model (henceforth the *constant density model*) consisting of 2D polygons with upper and lower boundaries based on the 4.0, 5.0, 6.0 and 7.0 km s^{-1} velocity contours, considered indicative of traditional oceanic crustal layering (White et al., 1992), and where model edge effects were prevented by extending the density structure for 1000 km beyond the model limits. As part of testing, the veracity of suspected inversion artefacts was also investigated at this point, particularly those located beneath the continental slope and transform fault regions of the model.

6.1. Initial modelling

As a starting point, the Carlson and Raskin (1984) standard velocity-density relationship for the oceanic crust was applied to construct the initial *constant density model*, with a density defined for each layer with depth within the crust of 2600, 2700, 2900 and 2950 kg m^{-3}, a density of 1030 kg m^{-3} assigned to the water column, and 3330 kg m^{-3} for the mantle. The expected FAA (Fig. 9c) was then calculated using *grav2d*, modified from the original programme written by J.H Luetgert based on the algorithm of Talwani et al. (1959), and compared to the observed FAA (Fig. 9c).

Although mirroring the general along-profile wavelength variation in the FAA, unsurprisingly given the simple starting density structure, a significant regional mismatch is observed with the calculated FAA being too high to the south of the SITF and too low to the north. We therefore divided this starting density-depth model into a series of lateral zones within which the density could be independently adjusted within each layer of each zone. Modelling was then progressed to determine the density-depth structure required to achieve the best fit to the observed anomaly (to within ±5 mGal error along the entire profile length), including regions poorly constrained by seismic ray coverage at the lateral extremities of the model.

6.2. Gravity fit

As a starting point for lateral and vertical density variation assignment along-profile, to the north of the SITF the velocity-density relationship of Carlson and Raskin (1984) was again applied for oceanic crust as a starting point,

even though it does not distinguish serpentinized mantle vs. mafic mantle or accommodate anomalously low-velocity or density fractured basalt. This model was chosen so that no preconceived idea for velocity-density-depth structure was imposed into the model initially, other than that of oceanic crust.

For the continental crust, in regions where the velocity is greater than 6 km s^{-1}, the relationship of Christensen and Mooney (1995) was applied, whilst considering the implications of the Carlson and Miller (2003) relationship for serpentinized mantle as applied in Prada et al. (2014). The Christensen and Mooney (1995) relationship is not applicable for velocities less than 6 km s^{-1}, so the relationship of Ludwig et al. (1970) was used for these regions of the model. The densities assigned to each of the 31 blocks for modelling, including incorporating a lateral density gradient within the mantle to match the longer wavelength component, are summarized in Table 2.

The calculated anomaly (Fig. 9c), although now a good fit along the majority of the profile, retains a mismatch in the region of the SITF. Consequently, further blocks were added vertically beneath the seabed extent of the SITZ (Fig. 9b) and the resulting fit to the observed FAA is shown in Figs 9c,d. To achieve this best fit (henceforth the *density model*) higher densities of 2700, 2800, 3000 and 3100 kg m^{-3} were required in these blocks.

6.3. Inversion artefacts

The best-fit *density model* was used to appraise the *P-wave* and *S-wave inversion models* to identify anomalies likely to be artefacts of the inversion process itself, such as velocity upward or downward smear, or a result of gaps in the ray coverage, such as that caused by OBSs 419 and 422 which did not record usable data. The primary areas of inversion artefact identified (Fig. 9b) are associated with deeper parts of the model, which gravity modelling suggests have more rapid lateral change in depth; for example, on the southern edge of the SITF (along-profile distance ~80 km) and where the continental-type crust appears to have undergone further thinning (along-profile distance 40-60 km). Here, the best-fit *density model* shows the more likely crustal structure.

However, for the shallower parts of the model the lateral variation in upper crustal structure appears to be real, since it is required to produce the shorter-wavelength fit between the observed and calculated anomalies. Of particular note are the two highs in the 5.5 km s^{-1} contour used to mark the top of the lower crust (Fig. 9b), that are required to match positive anomalies each of ~20 km wavelength in the observed FAA. Consequently, the *density model* is considered to be a valid, although smoothed, representation of the structure of the crust, and the *P-wave* and *S-wave inversion models* are considered valid for areas of any ray coverage, even those limited to less than 100 cell hits as part of inversion modelling (cf. Fig. 9b with Figs 5 & 6).

6.4 Along-flowline implications

Profile P04 runs MCSC-parallel off-axis through ~10 My-old oceanic lithosphere and both its *P-wave* and *S-wave inversion models* and the *density model* suggest along-axis variation in velocity and density structure, most likely inherited as part of oceanic crustal formation at the ridge axis. To investigate this inheritance, the regional satellite FAA (Fig. 10b – Sandwell and Smith v24 – Sandwell and Smith, 2009) was compared with the bathymetry in the first instance. To remove the effect of variable water depth, its contribution to the FAA was subtracted to yield the Bouguer anomaly (BA – Fig. 10b). Then a constant density, constant layer thickness oceanic crustal model, derived

from the *density model*, was used to calculate a crustal contribution which was subtracted to produce the mantle Bouguer anomaly (MBA – Fig. 10c) following the approach of Parker (1972).

Both the BA and MBA show that crustal formation at the MCSC appears to have been highly asymmetric both across- and along-axis for at least ~10-15 My, with positive anomalies concentrated on the western flank and in the northern section of the eastern flank, in the vicinity and to the north of the current location of the Mt Dent OCC. Positive anomalies in the BA and MBA would result from either the crust being thinner or more dense, or both, than that used to undertake the calculation (4 km and 2700 kg m^{-3} respectively). To consider the thermal affects associated with phases of magma-rich spreading, the thermal anomaly was calculated using the approach outlined in Peirce et al. (2001) and Peirce and Navin (2002), following the method of Forsyth (after Phipps Morgan and Forsyth, 1988; as developed from Forsyth and Wilson, 1984). When subtracted from the MBA, this results in the residual mantle Bouguer anomaly (RMBA – Fig. 10e). A further datum of 57.5 mGal was then subtracted to provide the RMBA residual (Fig. 10f), which more clearly shows areas of positive and negative anomaly that may indicate the distribution of crust formed under magma-poor and magma-rich conditions. Caution should be taken in interpreting the RMBA since the thermal structure applied represents the assumption of a predominance of magmatic accretion at the ridge axis when this may not have always been the case.

The region of crust suggested to have a magma-rich origin by the Vp/Vs ratio (~115 km to ~132 km along-profile distance), corresponds to a hiatus in the more positive anomaly regions in the RMBA residual. Consequently, it may also be used as an indicative proxy to show which crust within the wider Cayman Trough formed via magma-rich accretion, and which during a phase dominated by tectonism. In particular, the RMBA residual suggests that the MCSC in the vicinity of the Mt Dent OCC may currently be in a magma-rich phase, while the remainder of the ridge axis to within ~30 km of the SITF, is tectonically stretching. From here to the SITF, the RMBA residual suggests either a thicker crust or a lower density crust than that of the background calculation model. Since the *P-wave inversion model* does not suggest a much thinner crust in this region, this anomaly pattern may instead suggest that this part of the ridge axis, and the crust on both flanks, is cooler than further along-axis to the north. The corresponding blocks of the *density model* also have higher densities than those to the north which supports this conclusion.

7. MOHO – A BOUNDARY OR TRANSITION?

As a means of further testing the features of the inherently smoothed and interface-free *P-wave inversion model* and determining which velocity contour best represents the Moho and what its characteristics are along-profile, the *P-wave inversion model* was converted into a node-specified model with distinct layer boundaries incorporated. The 5.5 km s^{-1} velocity contour was used to define the upper-to-lower crust transition and the 7.0 km s^{-1} velocity contour chosen to represent the base of crust in the first instance (Fig. 11a). The observed first-arrival travel time picks (Pg and Pn phases) were then forward point-to-point ray-traced using *rayinvr* (Zelt and Ellis, 1988; Zelt and Smith, 1992 – Fig. 11b) to first appraise the validity of phase assignment, particularly given the effect of variation in seabed topography on arrival trend with offset within each record section, and then to further test the model fit and confirm the identification of likely artefacts (Fig. 9b).

Although the model (henceforth the *forward model*) is simpler in structure than its inversion equivalent, it still retains the lateral velocity anomalies in the upper crust, a thinned continental crust and a sharp lateral velocity transition associated with the SITF. The result of this modelling for OBSs 410, 420 and 430 is shown in Fig. 11b (ray diagram) and Figs 11c-e (travel time pick fits). As this modelling was undertaken to test where crustal layer interfaces might exist and what their characteristics are, ray-tracing was undertaken without adjusting any layer velocity or ascribed interface depth. Consequently, the resulting misfit should be regarded as indicative for all phase types combined, and not as the best fit that might be achieved if layer velocities and interfaces were further adjusted. The *forward model* has a T_{RMS} misfit of ~152ms and a χ^2 of ~9.2 for the ~21,900 travel time picks for all OBSs combined, with some individual instrument χ^2 fits as small as ~1.7. The larger misfits occur for OBSs located on the inside corner north of the SITZ, and for those in the shallowest water depths on the continental shelf.

The apparent absence of PmP phases to the north of the SITF may indicate that a distinct Moho interface may not exist with there instead being a transition zone from crust to mantle. Consequently, a forward predictive ray-tracing approach, tracing all potential PmP arrivals through the model, was also adopted not only to test the appropriateness of the selected base of crust marker (7.0 km s^{-1} velocity contour), but also the likelihood that it is a distinct interface rather than a transition zone, and if so, where it exists. The process was undertaken in two ways: i) tracing all possible PmP ray paths through the model – i.e. a predictive phase identification free approach; and b) point-to-point ray-tracing the picks identified as Pg, reassigned as Pn phases instead – i.e. only those that satisfy a Pn pathway through the model would be traced if the original identification was incorrect. Examples are shown in Fig. 11 for OBSs 410 (sited on oceanic crust), 420 (sited in the OCT) and 430 (sited on the continental margin) with the calculated phases also compared to the observed data in Figs 4b,d & e, respectively.

This modelling confirmed that PmP arrivals would only be observed to the south of the SITF. The implication of this result is that, elsewhere, either the Moho is a transition zone, or that the velocity contrast across the Moho is small, thus generating a PmP arrival amplitude indistinguishable above that of the background noise. Consequently, the 7.0 km s^{-1} contour can be regarded as marking the base of the crust where a distinct Moho exists and also the top of a gradient transition into the mantle elsewhere. Secondly, the modelling also suggests that, in the vicinity of SITF, the inversion modelling images the base of a zone of either lower crustal metamorphism or upper mantle serpentinization, with a thinner crust of higher density and velocity above, beneath the entire width of transform fault zone.

8. MODEL SIMILARITY AND UNIQUENESS

The *forward*, *P-wave and S-wave inversion* and *density models* are consistent within their associated uncertainties. As such, these models can be viewed, collectively, as a well-constrained and unique view of the sub-surface geological structure along a transect crossing the Cayman Trough, the Swan Islands Transform Fault Zone and Honduran continental margin. The features of these models will now be discussed in the context of both oceanic crustal accretionary processes on-going at the Mid-Cayman Spreading Centre and the evolution of transform continental margins. For this purpose, we assume that the 7.0 km s^{-1} velocity contour acts as a proxy for the base of crust along the entire profile. We also base crustal type identifications on a series of velocity-depth profiles taken at 5 km intervals through both P-wave models (Fig. 12a-e), by comparing them to standard velocity-depth

compilation envelopes [e.g. fracture zones – Minshull et al. (1991); oceanic crust – White (1979, 1984), as summarized in White et al. (1992) and Grevemeyer et al. (2018b); continental crust – as summarized in Peirce et al. (1996) and Greenroyd et al. (2007, 2008)].

8.1. P-wave inversion model

The *P-wave inversion model* (Fig. 8b) exhibits a generally smooth and interface-free velocity pattern that largely mirrors the seabed topographic highs and lows. The model can be divided into three primary domains based on velocity-depth profiles relating to continental-type crust to the south of the SITZ (~80 km along-profile distance – Fig. 12a), the SITF itself (~80 km to ~87 km along-profile distance – Fig. 12b), and the oceanic crust to the north. The oceanic domain can further be divided into three zones based on apparent crustal thickness variation and velocity within the upper crust (Figs 12c-e).

To the south of the SITF the continental crust appears to be, on average, ~14.5 km-thick to an along-profile distance of ~60 km, where it starts to thin quite rapidly to ~80 along-profile distance. Here the continental-type crust is ~10 km-thick and has a sharp, near-vertical transition located in the vicinity of a region observed at the seabed to be more densely faulted (Fig. 8a). Velocities beneath the seabed of 2.5 km s^{-1} suggest a sediment cover for most of this section of the model, with the transition between upper and lower crust marked by the 5.5 km s^{-1} velocity contour. The geometry of this contour suggests that the upper-to-lower crust transition may have a horst-graben-like structure, with the rapid lateral change in velocity suggesting that they are bounded by high-to-moderate angle normal faults. The consistent upper crustal velocity-depth structure beneath the continental margin implies that the variation in crustal thickness is accommodated by thinning of the lower crust. Due to the lack of ray coverage at the most southerly end of the model, gravity modelling better constrains the crustal thickness at ~23 km-thick at the southernmost end of the profile, and the stepped nature of the thinning northwards along profile implies that it may have occurred in multiple phases: firstly, to 23 km-thick associated with initial Honduran continental margin rifting; secondly, to ~14.5 km-thick over ~20 km beneath the current upper continental slope; and finally, to ~10 km-thick for ~30 km to the south of the SITZ, both of the latter associated with transform margin development.

The oceanic-type crust formed at the inside ridge-transform corner (~87 km to ~110 km along-profile distance – Fig. 12c), is the thinnest (~3 km) observed anywhere along-profile, which suggests that its formation process is different. Possible causes could be reduced mantle upwelling or that the ridge axis experienced a higher rate of cooling. Either heat conduction across the transform margin boundary, or enhanced hydrothermal circulation by fluid ingress into the transform fault system, or both, could result in such cooling. Moving northwards, between ~110 and ~135 km along-profile distance (Fig. 12d), here the oceanic crust is thickest (~5 km) and has higher velocity at shallower depths than observed elsewhere along the oceanic part of the profile. The additional crust appears to be related to a thicker section of lower crust. This structure suggests that this oceanic crust formed under more magma-rich conditions, and that the matching seabed topographic highs are volcanic in origin. Further north, for the remaining ~45 km along-profile (Fig. 12e), the velocity-depth structure is more consistent laterally, with an average crustal thickness of ~4 km. In general, at the seafloor velocities vary between 2.7 and between ~4.5 km s^{-1}, while at the bottom of the upper oceanic crust they range between 5.5 and 6.0 km s^{-1},

defined as the point of change in vertical gradient. The lower oceanic crust generally has velocities higher than, on average, 6.0 km s^{-1}. At the SITF (~80 to 87 km along-profile distance) the inversion suggests a very thin crustal section of ~2 km, as expressed by the very shallow depth of the 7.0 km s^{-1} velocity contour.

8.2. S-wave inversion model

The *S-wave inversion model* (Fig. 8c) exhibits a generally smooth and interface-free velocity pattern that also largely mirrors the seabed topographic highs and lows. The model can be divided into three domains, and the depth of the 7.0 km s^{-1} P-wave velocity contour again used to define the base of crust. This contour mirrors the 4.0 km s^{-1} S-wave velocity contour. Although generally more laterally variable, particularly in the lower crust, features are well resolved by ray coverage at a scale of 10 km-wide and 4 km-deep for the lower crust, and 4 km-wide by 2 km-deep for the upper crust (Fig. 7f,i). The most notable feature of this model is the region between ~115 km to ~135 km along-profile distance (Fig. 8d) that has elevated S-wave velocities at shallow crustal depths, and is interpreted as having formed during a magma-rich period based on the *P-wave inversion model*. In general, at the seafloor velocities vary between ~1.5 and ~2.5 km s^{-1}, while at the bottom of the upper oceanic crust they range between 2.5 and 3.0 km s^{-1}, based on the depth below seabed of the 5.5 km s^{-1} P-wave velocity contour. The lower oceanic crust generally has velocities higher than, on average, ~3.2 km s^{-1}. The lowest velocities observed along profile lie in the crust at what would have been, on axis, the transform fault-ridge axis intersection (~90 km to ~100 km along-profile distance – Fig. 8d), which may suggest that this area is pervasively cracked and fractured.

8.3. Comparison with CAYSEIS Profiles P02 and P06

Profile P04 intersects directly with Profile P06 (Grevemeyer et al., 2018a) at ~112 km along-profile distance (Figs 3 & 8). It also runs within ~20 km along-flowline distance of Profile P02 (Harding et al., 2017) at ~137 km along-profile distance. The analysis of the seismic data acquired along both of these profiles was undertaken by tomographic inversion and so it is appropriate to compare their models with the *P-wave inversion model* to determine consistency. The comparison with Profile P06 at the intersection point is shown in Fig. 8c, and with the extrapolation of the end of Profile 02 in Fig. 8e. Given that the modelling has been undertaken independently using three different tomographic approaches, these models are remarkably consistent, which adds confidence to their uniqueness.

Focusing on the intersection of Profiles P04 and P06, Grevemeyer et al. (2018a) conclude that the crust lies within the transition between a phase of magma-rich to magma-poor formation, with the crust to the west of Profile P04 progressively thinning and to the east thickening, largely by a thickening of the lower crust. This provides a three-dimensional perspective of a waxing and waning magma supply and not simply a focused delivery to the ridge axis. It also suggests a component of along-axis migration, or flow, associated with more magma-rich periods, since this apparently magma-rich region along Profile P04 occupies a mid-segment setting. Consequently, the birth and death of OCCs formed at the ridge axis may be triggered by the episodic arrival of magma, and the distance over which it can migrate along-axis; the OCCs developing at that limit as the influx wanes. This may explain why the OCCs observed to date (either active or inactive and preserved off-axis) are found to the north along-axis, since the RMBA residual suggests a more northerly focus of magma replenishment. This conclusion is

consistent with the interpretation of the crustal model for along-axis Profile P01, which shows thicker crust to the south of the Mt Dent OCC and suggests a recent magma event underlying the Beebe Vent field (Van Avendonk et al., 2017).

8.4 Forward model

The *forward model* (Fig. 11a) comprises two main structural subdivisions: continental crust between 0 km to ~80 km along-profile distance, and oceanic crust at greater profile distances. The OCT is marked by an ~10 km-wide SITF that is characterized by a higher velocity at shallower depth than observed in the crust on either side, and a rapid lateral change in velocity particularly within the lower crust. The corresponding bathymetry (Fig. 8a) suggests that the fault may not only have a component of left-lateral movement, but also a displacement in the north-south direction, making this a ~10 km-wide trans-tensional system with an abrupt transition to the adjacent margin crust contained largely within the lower crust.

In turn, the density anomaly suggests that this fault zone enables significant water ingress into the lower crust and uppermost mantle facilitating metamorphism, with fracturing within a relatively narrow and sub-vertical network effectively blocking the transmission of S-waves propagating from shots fired to the north of the SITF. Such a fault network would explain why Sn arrivals are not observed, despite the better sensor coupling to the seabed due to the thin covering of sediment on the continental slope.

South of the SITF, the continental margin crust has a maximum thickness of ~19 km at ~30 km along-profile distance at the limit of the ray coverage, while the *density model* suggests the crust reaches a thickness of ~23 km by the southern end of the profile. This thinning of ~14 km over a distance of ~80 km, is largely accommodated by thinning of the lower crust. Although not required by either seismic model to achieve a good fit, gravity modelling suggests that the base of the crust beneath the continental slope may have a step-like geometry.

The velocities increase from <2.5 km s^{-1} at the seafloor to 7.0 km s^{-1} at the Moho which is higher than expected for continental crust (after Christensen and Mooney, 1995) and may be evidence for terrains having been accreted to the Honduras margin. When compared to standard continental velocity-depth envelopes (e.g. Christensen and Mooney, 1995) the crust is identified as thinned continental in type (Fig. 12a,b), and is consistent with global averages in continental margin settings (e.g. Peirce et al., 1996; Greenroyd et al., 2007, 2008).

The oceanic crust has a relatively consistent thickness in velocity-depth profiles along-profile (Fig. 12c-e), at ~4.0 km on average towards the north and ~5.0 km on average towards the SITF (inside corner). At the seafloor, velocities vary between 2.7 and between ~4.5 km s^{-1}, while at the bottom of the upper oceanic crust they range between 5.5 and 6.0 km s^{-1}. The lower oceanic crust has a velocity of 6.0 km s^{-1} in its upper part.

8.5. Differences between P-wave inversion and forward models

Although the forward modelling was only undertaken to test the result of the interface-free inversion approach and identify likely artefacts, the *P-wave inversion* and *forward models* do have notable differences (Fig. 13) where the velocity contrast at equivalent crustal depth exceeds ±0.5 km s^{-1}. The primary differences are located in the upper-to-lower crustal transition between the continental slope where the *forward model* suggests higher velocities than the *P-wave inversion model*. However, this upper crustal increase is mirrored in the lower crust of the *P-wave*

inversion model by a higher velocity than the *forward model* – interpreted as a compensation feature commonly observed in inversion-derived models. Generally, throughout the oceanic crust the *P-wave inversion model* tends to show higher velocities except in the region of crust considered likely to have had a more magma-rich formation.

9. DISCUSSION

9.1. Oceanic crustal accretion at the Mid-Cayman Spreading Centre

Recent studies conducted within the *CAYSEIS* context (Harding et al., 2017; Van Avendonk et al., 2017; Grevemeyer et al., 2018a) conclude that oceanic crustal formation at the MCSC is dependent on a temporal fluctuation of magmatism, reflecting the change from magma-rich to magma-poor spreading conditions over several million years. Harding et al. (2017) propose that a pulse of on-axis magmatism at about 2 Ma generated the Von Damm vent field, an axial-flank hydrothermal vent near the summit of the Mt Dent oceanic core complex. Prior to this magmatic pulse, magmatism in this central portion of the MCSC was low and seafloor spreading produced either thin crust or smooth, mantle-dominated seafloor. Van Avendonk et al. (2017) conclude that MCSC magmatism has been intermittent, or episodic, for the last 20 My with the seismic crustal structure of the axial valley showing two magmatic-tectonic segments along-axis. In a separate investigation, based on geological information at the seafloor, Haughton et al. (2019) hypothesize that magmatic intrusions propagated southward along the northern axial volcanic ridge and intersect Mt Dent. Haughton et al. (2019) also propose that the seafloor immediately to the east of Mt Dent is volcanic and possibly formed by magmatic events that crosscut, and potentially deactivate, the detachment.

In contrast with Haughton et al.'s (2019) hypothesis for the region east of Mt Dent, Van Avendonk et al.'s (2017) velocity-depth model suggests that exhumed mantle exists at the boundary between the two segments, while volcanic crust occupies most of the axial valley seafloor, as shown by the gradual increase in seismic velocity to 7.5 km s^{-1} at a depth of 5 km close to Mt Dent, that is interpreted as unroofed and partially hydrated mantle rocks rather than new igneous basement. This observation agrees with Hayman et al. (2011), who report that serpentinites were recovered from the seafloor in the vicinity. According to Hayman et al. (2011), the 2 My-old basement of Mt Dent consists of mantle rocks intruded by gabbros, with an inward-dipping detachment fault marking the western rift valley wall, exhuming plutonic and upper mantle rocks as an OCC. This detachment fault may have facilitated water ingress and deep hydration of the lithosphere of the axial valley adjacent to the OCC. Van Avendonk et al. (2017) postulate that fault slip, either on this detachment or on new normal faults dissecting the OCC, could accommodate the current extension across the central MCSC. Furthermore, the presence of low-velocity zones within the two spreading regions is also noted, which are interpreted as mush zones resulting from an along-axis magma migration, consistent with abundant volcanic rock outcrops in the axial basins (Hayman et al., 2011).

Grevemeyer et al. (2018a) show that seafloor spreading dynamics at the MCSC switched between episodic phases of magma-rich and magma-poor oceanic crustal formation, including exhumation of serpentinized mantle. Using a Vp/Vs of 1.9 to discriminate between serpentinized mantle ($\geq$1.9) and magmatically accreted crust (<1.9), they conclude that to the west of the ridge axis seafloor younger than 10 My has been magmatically accreted, while older seafloor is characterized by exhumation of serpentinized peridotite. Each phase of magma-rich and magma-poor formation lasts about 2 My. The eastern ridge flank exhibits, overall, features similar to those of the western

flank, although the durations of periods of magma-rich versus magma-poor spreading are distinctly different.

Consistent with previous studies conducted at the ultraslow MCSC (e.g. Ewing et al. 1960; White et al., 2001; ten Brink et al., 2002; Harding et al., 2017; Van Avendonk et al., 2017; Grevemeyer et al., 2018a), our results show a generally thin oceanic crust (~4 km-thick) along the ~10 My isochron, suggesting that it formed during dominantly magma-poor/tectonic spreading conditions. However, between ~115 km and ~132 km along-profile distance, a localized period of magma-rich crustal formation appears to have occurred during this time. The velocity-depth crustal structure supports this observation, with higher velocities correlating with topographic highs that have been interpreted as volcanic in origin, and a Vp/Vs ratio similarly having an along-axis variation (Fig. 8). The apparent absence of PmP arrivals suggests a transition zone into the oceanic mantle, which could be interpreted as a consequence of water ingress down detachments and metamorphism of the lower crust/upper mantle. These same detachments may also have exposed mantle peridotite at the seafloor.

Following Grevemeyer et al.'s (2018a) approach, we use the Vp/Vs ratio to distinguish between serpentine- vs. non–serpentine-dominated crust (Fig. 8f) in addition to a more gradual corresponding increase in velocity with depth. We show that, off-axis, a 1.9 Vp/Vs discriminator remains valid and that it may also be used to mark the transition between upper and lower crust. The *Vp/Vs model* (Fig. 8f) also shows that the bathymetric highs along Profile P04 are volcanic constructs.

Our observations suggest that magmatic accretion may not only be episodic in the across-axis direction (Grevemeyer et al., 2018a), but is also similarly focused, or episodic, in the along-axis direction, with the ridge-transform intersection (now relict at ~10 My off-axis) being tectonically dominated. This hypothesis of very focused magma delivery along-axis, such that regions of tectonic and magmatically formed crust may be inter-dispersed, would be consistent with observations of ultramafic and mafic gabbroic rocks dredged from the seabed (Hayman et al., 2011).

Adjacent to the SITF, our model shows that thin tectonized oceanic crust or serpentinized mantle abuts against thinned continental crust across a sharp transition located at the approximate centre of the bathymetric depression. This suggests that repeated earthquake rupture is focused along this very narrow zone along which several tens of kilometres of rupture occurs. As such, the transform fault represents a highly tectonized transition zone to the oceanic crust to the north. This interpretation is supported by the high velocity/high density correlation, which could be explained as zone of fracturing acting as a conduit for fluid that has altered both crustal and uppermost mantle rocks.

9.2 Swan Islands transform ocean-continental margin

Beneath the Swan Islands (Honduran) margin seismic modelling shows that the continental crust is relatively thin at ~15-18 km-thick below effectively the entire shelf and slope region, when compared to that expected (Fig. 12a,b). The *density model*, which provides better constraint on crustal thickness at the southern limit of the model, suggests the crust is 23 km-thick. At its thinnest adjacent to the SITF, the continental crust is ~10 km-thick having further thinned by 13 km over a distance of ~80 km; yielding a thinning of more than 50% over this distance.

Such continental crustal thinning is supported by Sanchez et al. (2016), who analyse satellite potential field data to conclude that generally low Bouguer anomalies represent thicker crust under the margin relative to further

offshore. Their modelling suggests a progressive increase in crustal thickness from around 5-10 km in the Cayman Trough, to 20-25 km in the northern Honduran borderlands. In addition, Sanchez et al. (2016) also study the continental crustal characteristics in the southern Honduran borderlands and interpret the thin crust revealed by the gravity and magnetic data as resulting from rifting associated with Jurassic and Cretaceous extension, driven by the proto-Caribbean rifting and oceanic spreading that developed as the North American and South American plates moved apart. However, continental crustal thinning can be dramatically different between transform margins as shown by several studies conducted at margins in stage 3 (passive stage) of their evolution, where gravity and wide-angle seismic models suggest that the continental crust thins sharply over a distance of less than 10-40 km. For example, the Barents Sea-Svalbard (Faleide et al., 1991), Ghana (Edwards et al., 1997), Grand Banks (Keen et al., 1990), North Atlantic (Fox and Gallo, 1986) and Exmouth Plateau (Lorenzo et al., 1991) margins exhibit continental crustal thinning over zones of 10-20, 15 and 40 km-wide. Edwards et al. (1997) also note that the Ghana ocean-continent boundary is characterized by high density (3100 kg m^{-3}), high velocity (5.8-7.3 km s^{-1}) and high magnetization (1.10-1.25 A m^{-1}). They suggest that this zone may be a consequence of either intrusion by basic igneous rocks or serpentinization of upper mantle material.

In the case of the SITF, the OCT is characterized by high velocity at shallower depths similar to Edwards et al.'s (1997) model for the Ghana margin, and by high densities. We explain the high-density anomaly to result from water ingress into the lower crust and uppermost mantle through the fracture system, facilitating metamorphism, with fractures concentrated within a relatively narrow and sub-vertical network. Contrasting conclusions are drawn by Greenroyd et al. (2007, 2008), who studied two profiles offshore French Guiana, crossing the French Guiana continental margin and the Demerara Plateau. Here the pre-rift continental crust is 35-37 km-thick, while at the oceanward end of each transect the oceanic crust is 3.5-5.0 km-thick. At the Demerara Plateau the continental crust thins abruptly over a distance of 70 km, adjacent to a 45 km-wide ocean-continent transition zone. Offshore French Guiana more gradual thinning occurs over 320 km adjacent to an abrupt transition to oceanic crust. Greenroyd et al. (2007, 2008) explain such wide zones of continental crustal thinning as resulting from trans-tensional motion.

At the SITF, continental crustal thinning occurs over a distance of ~80 km adjacent to a sharp OCT <10 km-wide. However, in contrast to the margins described above, the SITF is currently an active transform margin, across which the plates continue to drift with a prevalent left-lateral strike-slip motion as evidenced by earthquake focal mechanisms (Hayman et al., 2011; Graham et al., 2012). Thinned old continental crust, resulting from the Jurassic/Cretaceous rifting process (Sanchez et al., 2016) is, thus, then juxtaposed against very thin and young oceanic crust formed at the MCSC. The thin oceanic crust adjacent to the SITF could, therefore, be the consequence of a reduction in melt generation at the ultraslow Mid-Cayman Spreading Centre as a result of conductive heat loss in the slowly rising mantle, or due to a reduced magma budget at the tips of the ridge segments adjacent to oceanic fracture zones (White et al., 1984, 1992; Minshull et al., 1991).

9.3 Larger-scale processes

Our modelling suggests that the continental crust of the Honduran margin was most likely already thinned prior to onset of transform margin development, with there being no evidence for that rifting taking place in a magma-enhanced stretching environment. Our modelling also suggests that on-going transform margin formation further

stretched this crust to less than half of its pre-transform margin initiation thickness. Consequently, at the Swan Islands margin at least, ocean-continent transform development involved stretching of the adjacent continental crust.

Furthermore, the oceanic crust that formed in the inside corner position of the intersection between the transform fault system and the ridge axis, occurred in a magma-poor environment (Reston et al., 2009). This may have resulted from reduced mantle upwelling or enhanced cooling either by the adjacent older, cold continental crust or by an enhanced fluid cooling system, able to reach a significant depth as a result of the fracturing and faulting associated with transform motion, which appears to have had a trans-tensional component.

10. CONCLUSIONS

New velocity-depth and density-depth models for the Swan Island transform margin have been presented for an ~180 km-long transect that also traverses ~10 My-old oceanic crust generated at the Mid-Cayman Spreading Centre. These models are consistent and robustly tested and we summarize their interpretation as follows:

1) the oceanic crust accreted at the ultraslow MCSC is ~4 km-thick and most likely formed during a period of predominantly magma-poor/tectonic spreading both along- and across-axis;
2) Vp/Vs ratio variation along-profile suggests focused and episodic magma-rich crustal formation within a 20 km-wide region corresponding with off-axis bathymetric highs, making them most likely volcanic in origin;
3) off-MCSC-axis, a Vp/Vs ratio of 1.9 is a valid discriminator between serpentine- vs. non-serpentine-dominated crust as well as a discriminant between upper and lower crust;
4) in between the OCCs the crust appears to have been magmatically accreted and, given the crustal thickness, under "just enough" magmatic conditions suggesting, in turn, focussed magma delivery to the ridge axis;
5) the continental crust beneath the Honduran margin is thin, and thins in multiple phases by a further ~13 km over a distance of ~80 km towards the SITF;
6) the SITF is an ~5-10 km-wide fault zone at the southern edge of the Cayman Trough crust, bound to the south by a sharp transition between oceanic- and continental-type crusts; and
7) the Swan Island stage 2 (drifting) transform continental margin is characterized by a ~20 km-wide trans-tensional system, that accommodates left-lateral strike-slip motion between North American and Caribbean plates, and has corresponding higher velocity and density anomalies within the crust.

ACKNOWLEDGMENTS

We thank the officers, engineers and crew of the F/S Meteor for their support during the M115 *CAYSEIS* cruise. Funding for this project was provided by the UK's Natural Environment Research Council (NERC) under grant NE/K011162/1 to Durham University, the US National Science Foundation (NSF) under grant OCE-1356895 to the University of Texas Austin (UTIG), and to GEOMAR by the German Research Foundation (DFG). Hayman was serving as a Program Director at the NSF during preparation of this manuscript. The wide-angle seismic data were recorded with instruments provided by UTIG and GEOMAR, as well as NERC's Ocean-Bottom

Instrumentation Facility (Minshull et al., 2005). We thank their technical teams for their professional support. The ship-based gravimeter was provided by the NERC's National Marine Equipment Facility, together with its installation technical support. The seismic data used in this study are available at the Academic Seismic Portal at UTIG (www-udc.ig.utexas.edu/sdc), the World Data Center PANGAEA (www.pangaea.de), and the British Oceanographic Data Centre (www.bodc.ac.uk). All figures were prepared using the Generic Mapping Tools (GMT) package (Wessel and Smith, 1998). We thank the reviewers for their helpful comments. The manuscript of this paper is deposited in Durham University's open access publication repository, Durham Research Online (DRO – dro.dur.ac.uk).

REFERENCES

Basile, C., Mascle, J., Benkhelil, J. and Bouillin, J.-P., 1998. Geodynamic evolution of the Cote d'Ivoire-Ghana transform margin: An overview of Leg 159 results. In: Mascle, J., Lohmann, G.P. and Moullade, M. (eds.), *Proc. ODP, Sci. Results*, 159, 101-110.

Blarez, E. and Mascle, J., 1988. Shallow structure and evolution of the Ivory Coast and Ghana transform margin. *Mar. Petr. Geol*., 5, 54-64.

Boschman, L. M., van Hinsbergen, D. J. J., Torsvik, T. H., Spakman, W., and Pindell, J. L., 2014. Kinematic reconstruction of the Caribbean region since the Early Jurassic. *Earth Science Revs.*, 138, 102-136, https://doi.org/10.1016/j.earscirev.2014.08.007.

Carlson, R.L. and Miller, D.J., 2003. Mantle wedge water contents estimated from seismic velocities in partially serpentinized periodotites. *Geophys. Res. Letts*., 30(5), https://doi.org/10.1029/2002GL016600.

Carlson, R.L. and Raskin, G.S., 1984. Density of the ocean crust. *Nature*, 311, 555-558.

Christeson, G.L., Gulick, S.P., Van Avendonk, H.J., Worthington, L.L., Reece, R.S. and Pavlis, T.L., 2010. The Yakutat terrane: Dramatic change in crustal thickness across the Transition fault, Alaska. *Geology*, 38(10), 895-898.

Christensen, N.I., 2004. Serpentinites, peridotites and seismology. *Int. Geol. Rev*., 46, 795-816.

Christensen, N.I. and Mooney, W.D., 1995. Seismic velocity structure and composition of the continental crust: a global view. *J. geophys. Res*., 100(B6), 9761-9788.

Connelly, D.P., Copley, J.T., Murton, B.J., Stansfield, K., Tyler, P.A., German, C.R., Van Dover, C.L., Amon, D., Furlong, M., Grindlay, N. and Hayman, N., 2012. Hydrothermal vent fields and chemosynthetic biota on the world's deepest seafloor spreading centre. *Nature Communications*, 3, 620.

Dalziel, I.W.D. and Dewey, J.F., 2018. The classic Wilson cycle revisited, *in* Wilson, R.W., Houseman, G.A., McCaffrey, K.J.W., Doré, A. G., and Buiter, S. J. H. (eds.), Fifty years of the Wilson cycle concept in plate tectonics. *Geol. Soc. Spec. Pub*., 470, in press, https://doi.org/10.1144/SP470.1.

DeMets, C., Mattioli, G., Jansma, P., Rogers, R., Tenorio, C. and Turner, H.L, 2007. Present motion and deformation of the Caribbean plate: Constraints from new GPS geodetic measurements from Honduras and Nicaragua. *Geol. Soc. Am. Spec. Pub.*, 428, 21-36.

Detrick, R.S., White, R.S. and Purdy, G.M, 1993. Crustal structure of North Atlantic Fracture Zones. Rev. *Geophys*., 31, 439-458.

Dick, J.J.B., Lin, J. and Schouten, H., 2003. An ultraslow-spreading class of ocean ridge. *Nature*, 426, 405-411.

Edwards, R.A., Whitmarsh, R.B. and Scrutton, R.A, 1997. The crustal structure across the transform continental margin off Ghana, eastern equatorial Atlantic. *J. geophys. Res*., 102(Bl), 747-772.

Escartin, J., Hirth, G. and Evans, B., 1997. Nondilatant brittle deformation of serpentinites: Implications for Mohr-Coulomb theory and the strength of faults. *J. geophys. Res*., 102, 2897-2913, https://doi.org/ 10.1029/96JB02792.

Ewing, J., Antoine, J. and Ewing, M., 1960. Geophysical measurements in the western Caribbean Sea and in the Gulf of Mexico. *J. geophys. Res*., 65, https://doi.org/10.1029/JZ065i012p04087.

Feleide, J.I., Gudlaugsson, S.T., Eldholm, O., Myhre, A.M. and Jackson, H.R., 1991. Deep seismic transects across the sheared western Barents Sea-Svalbard continental margin. *Tectonophysics,* 189, 73-89.

Forsyth, D.W. and Wilson, B., 1984. Three dimensional temperature structure of a ridge-transform-ridge system. *Earth Planet. Sci. Lett*., 70, 355-362.

Fox, P.J. and Gallo, D.G., 1986. The geology of North Atlantic transform plate boundaries and their aseismic extensions. In: Vogt, P.R. & Tucholke, B.E. (eds.), The Geology of North America, vol. M, The western North Atlantic Region, *Geol. Soc. Am*., 157-172.

Francheteau, J. and Le Pichon, X., 1972. Marginal fracture zones as structural framework of continental margins in South Atlantic Ocean. *AAPG Bulletin*, 56, 991-1007.

Gadd, S.A. and Scrutton, R.A., 1997. An integrated thermomechanical model for transform continental margin evolution. *Geo. Mar. Letts*., 17, 21-30.

German, C.R., Bowen, A., Coleman, M.L., Huber, J.A., Seewald, J., Van Dover, C., Whitcomb, L.L., Yoerger, D., Connelly, D., Honig, D.L., Jakuba, M., Kinsey, J.C., McDermott, J., Nakamura, K., Sands, C., Smith, J. and Sylva, S., 2009. Hydrothermal exploration of the Mid-Cayman Spreading Centre: isolated evolution on Earth's deepest Mid-Ocean Ridge. AGU Fall Meeting, Session OS21B-08.

Graham, S.E., DeMets, C., DeShon, H.R., Rogers, R., Rodriguez Maradriaga, M., Strauch, W., Wiese, K. and Hernandez D., 2012. GPS and seismic constraints on the M=7.3 2009 Swan Islands earthquake: implications for stress changes along the Motagua fault and other nearby faults. *Geophys. J. Int*., 190, 1625-1639.

Greenroyd, C.J., Peirce, C., Rodger, M., Watts, A.B. and Hobbs, R.W., 2007. Crustal structure of the French Guiana margin, West Equatorial Atlantic. *Geophys. J. Int*., 169, 964-987.

Greenroyd, C.J., Peirce, C., Rodger, M., Watts, A.B. and Hobbs, R.W., 2008. Demerara Plateau – the structure and evolution of a transform passive margin. *Geophys. J. Int*., 172, 549-564.

Grevemeyer, I., Dannowski, A., Hayman, N.W., Peirce, C. and Van Avendonk, H., 2016. *CAYSEIS* – magma-starved oceanic crustal accretion and transform margin formation in the Cayman Trough revealed by seismic and seismological data. FS Meteor M115 cruise report (unpublished), pp92.

Grevemeyer, I., Hayman, N.W., Peirce, C., Schwardt, M., van Avendonk, H., Dannowski, A. and Papenberg, C., 2018a. Episodic magmatism and serpentinized mantle exhumation at an ultraslow spreading centre. *Nature Geoscience*, https://doi.org/10.1038/s41561-018-0124-6.

Grevemeyer, I., Ranero, C.R. and Ivandic, M., 2018b. Structure of oceanic crust and serpentinization at subduction zones. *Geosphere*, 14(2), https://doi.org/110.1130/GES01537.1.

Harding, J.L., Van Arendonk, H.J.A., Hayman, N.W., Grevemeyer, I. and Peirce C., 2017. Magmatic-tectonic conditions for hydrothermal venting on an ultraslow-spread oceanic core complex. *Geology*, 45, 839-842.

Haughton, G., Hayman, N.W., Searle, R.C., Le Bas, T. and Murton, B.J., 2019. Volcanic-tectonic structure of the tent oceanic core complex in the ultraslow Mid-Cayman Spreading Center determined from detailed seafloor investigation. *Geochem. Geophys. Geosyst*., https://doi.org/10.1029/2018GC008032.

Hayman, N.W., Grindlay, N.R., Perfit, M.R. and Mann, P., 2011. Oceanic core complex development at the ultraslow spreading Mid-Cayman Spreading Centre. *Geochem. Geophys. Geosyst*., 12(3), https://doi.org/10.1029/2010GC003240.

Holcombe, T.L. and Sharman, G.F., 1973. Post-Miocene Cayman Trough evolution: a speculative model. *Geology*, 11, 714-717.

Horen, H., Zamora, M. and Dubuisson, G., 1996. Seismic wave velocities and anisotropy in serpentinized peridotites from Xigaze ophiolite: abundance of serpentine in slow spreading ridge. *Geophys. Res. Letts*., 23, 1, 9-12.

Keen, C.E., Kay, W.A. and Roest, W.R., 1990. Crustal anatomy of a transform continental margin. *Tectonophysics,* 173, 527-544.

Kuna, V.M., Nábělek, J.L. and Braunmiller, J., 2019. Mode of slip and crust–mantle interaction at oceanic transform faults. *Nature Geoscience*, 12, 138-142, https://doi.org/10.1038/s41561-018-0287-1.

Lavier, L.L. and Manatschal, G., 2006. A mechanism to thin the continental lithosphere at magma-poor margins. *Nature*, 440(7082), 324-328, https://doi.org/10.1038/nature04608.

Le Pichon, X. and Hayes, D., 1971. Marginal offsets, fracture zones and the early opening of the south Atlantic. *J. Geophys. Res*., 76, 6283-6293.

Leroy, S., Mauffret, A., Patriat, P. and Mercier de Lepinay, B., 2000. An alternative interpretation of the Cayman Trough evolution from a re-identification of magnetic anomalies. *Geophys. J. Int*., 141, 539-557.

Lorenzo, J.M. and Vera, E.E., 1992. Thermal Uplift and Erosion across the Continent-Ocean Transform Boundary of the Southern Exmouth Plateau. *Earth Planet. Sci. Lett*., 108, 79-82.

Lorenzo, J.M., Mutter, J.C., Larson, R.L. and the Northwest Australia Study Group, 1991. Development of the continent-ocean transform boundary of the southern Exmouth Plateau. *Geology*, 19, 843-846.

Ludwig, J.W., Nafe, J.E. and Drake, C.L., 1970, Seismic refraction. In: Maxwell A.E. (ed.), The Sea, Wiley-Interscience, 53-84.

Mann, P., 2007. Overview of the tectonic history of northern Central America. In: Mann, P. (ed.), Geologic and tectonic development of the Caribbean plate boundary in northern Central America, *Geol. Soc. Am. Spec. Pub*., 428, 1-19, https://doi.org/10.1130/2007.2428(01).

Mascle, J., 1976. Atlantic-type continental margins – Distinction of two basic structural types. *Anais da Academia Brasileira de Ciencias*, 48, 191-197.

Mascle, J. and Blarez, E., 1987. Evidence for transform margin evolution from the Ivory Coast -Ghana continental margin. *Nature*, 326, 378-381.

Mascle, J., Lohmann, P. and Clift, P., 1997. Development of a passive transform margin: Cote d'Ivoire-Ghana transform margin- ODP Leg 159 preliminary results. *Geo. Mar. Letts*., 17(1), 4-11.

Mercier de Lépinay, B., Deschamps, A., Klingelhoefer, F., Mazabraud, Y., Delouis, B., Clouard, V., Hello, Y., Crozon, J., Marcaillou, B., Graindorge, D., Vallée, M., Perrot, J., Bouin, M. P., Saurel, J. M., Charvis, P., and St-Louis, M., 2011. The 2010 Haiti earthquake: A complex fault pattern constrained by seismologic and tectonic observations. *Geophys. Res. Letts*., 38, 22305, https://doi.org/10.1029/2011GL049799.

Mercier De Lepinay, M., Loncke, L., Basile, C., Roest, W., Patriat, M., Maillard, A. and De Clarens, P., 2016. Transform continental margins – Part 2: A worldwide review. *Tectonophys*., 693, 96-115.

Minshull, T.A., White, R.S., Mutter, J.C., Buhl, P., Detrick, R.S., Williams, C.A. and Morris, E., 1991. Crustal Structure at the Blake Spur Fracture Zone from Expanding Spread Profiles. *J. geophys. Res.,* 96(B6), 9955-9984.

Minshull, T.A., Sinha, M.C. and Peirce, C., 2005. Multi-disciplinary, sub-seabed geophysical imaging: A new pool of 28 seafloor instruments in use by the United Kingdom Ocean Bottom Instrument Consortium. *Sea Technology*, 46(10), 27-31.

Müller, M.R., Minshull, T.A. & White, R.S., 2000. Crustal structure of the Southwest Indian Ridge at the Atlantis II fracture zone. *J. geophys. Res*., 105(B11), 25809-25828.

Müller, R.D., Sdrolias, M., Gaina, C. and Roest, W.R., 2008. Age, spreading rates, and spreading asymmetry of the world's ocean crust. *Geochem. Geophys. Geosyst*., 9, https://doi.org/10.1029/2007GC001743.

Olive, J.A., Behn, M.D. and Tucholke, B.E., 2010. The structure of oceanic core complexes controlled by the depth distribution of magma emplacement. *Nature Geoscience*, 3(7), 491.

Parker, R.L., 1972. The rapid calculation of potential anomalies. *Geophys. J. R. astr. Soc*., 31, 447-455.

Peirce, C., 2015. *CAYSEIS* – Crustal accretion and transform margin evolution at ultraslow spreading rates. FS Meteor M115 NERC cruise report (unpublished), pp41.

Peirce, C. and Navin, D.A., 2002. The RAMESSES experiment – V. Crustal accretion at axial volcanic ridge segments – a gravity study at 57°45'N on the slow spreading Reykjanes Ridge. *Geophys. J. Int*., 149, 76-94.

Peirce, C., Whitmarsh, R.B., Scrutton, R.A., Pontoise, B., Sage, F. and Mascle, J., 1996. Cote d'Ivoire-Ghana margin: seismic imaging of passive rifted crust adjacent to a transform continental margin. *Geophys. J. Int*., 125, 781-795.

Peirce, C., Turner, I.M. and Sinha, M.C., 2001. Crustal structure, accretionary processes and rift propagation: a gravity study of the intermediate-spreading Valu Fa Ridge. Lau Basin, *Geophys. J. Int*., 146, 53-73.

Peirce, C., Reveley, G., Robinson, A.H., Funnell, M.J., Searle, R.C., Simão, N.M., MacLeod, C.J. and Reston, T.J., 2019. Constraints on crustal structure of adjacent OCCs and segment boundaries at 13°N on the Mid-Atlantic Ridge. *Geophys. J. Int*., https://doi.org/10.1093/gji/ggz074.

Phipps Morgan, J. and Forsyth, D.W., 1988. Three-dimensional flow and temperature perturbations due to a transform offset: effects on oceanic crustal and mantle structure. *J. geophys. Res.*, 93, 2995-2966.

Prada, M., V. Sallares, C. R. Ranero, M. G. Vendrell, I. Grevemeyer, N. Zitellini, and R. de Franco, 2014. Seismic structure of the Central Tyrrhenian basin: Geophysical constraints on the nature of the main crustal domains. *J. Geophys. Res*., 119, 52-70, https://doi.org/10.1002/2013JB010527.

Reston, T.J., 2009. The structure, evolution and symmetry of the magma-poor rifted margins of the North and Central Atlantic: A synthesis. *Tectonophys*. 468, 6-27.

Rogers, R.D., Mann, P. and Emmet, P.A., 2007a. Tectonic terranes of the Chortis block based on integration of regional aeromagnetic and geologic data. In: Mann, P., *Geologic and Tectonic Development of the Caribbean Plate Boundary in Northern Central America*. *Special Papers-Geological Society of America*. **428**. 66-88, https://doi.org/10.1130/2007.2428(04).

Rogers, R., Mann, P., Emmet, P., and Venable, M., 2007b. Colon fold-thrust belt of Honduras: Evidence for late Cretaceous collision between the continental Chortis block and intra-oceanic Caribbean arc. In: Mann, P. (ed.), Geologic and tectonic development of the Caribbean plate in northern Central America, *Geol. Soc. Am. Spec. Pub*., 428, 129-150, https://doi.org/10.1130/2007.2428(06).

Rosencrantz, E. and Mann, P., 1991. SeaMarc II mapping of transform faults in the Cayman Trough, Caribbean Sea. *Geology*, 19, 690-693.

Rosencrantz, E., Ross, M. and Sclater, J.G., 1988. Age and spreading history of the Cayman Trough as determined from depth, heat flow, and magnetic anomalies. *J. geophys. Res*., 93(B3), 2141-2157.

Sage, F., Basile, C., Mascle, J., Pontoise, B. and Whitmarsh, R.B., 2000. Crustal structure of the continent–ocean transition off the Côte d'Ivoire–Ghana transform margin: implications for thermal exchanges across the palaeotransform boundary. *Geophys. J. Int*., 143, 662-678.

Sanchez, J., Mann, P. and Emmet, P.A., 2016. Late Cretaceous–Cenozoic tectonic transition from collision to transtension, Honduran Borderlands and Nicaraguan Rise, NW Caribbean Plate boundary. In: Nemčok, M., Rybar, S., Sinha, S.T., Hermeston, S.A. and Ledvenyiova, L. (eds.), Transform Margins: Development, Controls and Petroleum Systems, *Geol. Soc. Lond. Spec. Pub*., 431, 273-297, https://doi.org/10.1144/SP431.3.

Sandwell, D.T. and Smith, W.H.F., 2009. Global marine gravity from retracked Geosat and ERS-1 altimetry: ridge segmentation versus spreading rate. *J. geophys. Res*., 114, https://doi.org/10.1029/2008JB006008.

Scrutton, R.A., 1979. On sheared passive continental margins. *Tectonophys*., 59, 293-305.

Searle, R.C., 2012. Multiple seafloor spreading modes in the Mid-Cayman Spreading Centre. AGU Fall Meeting, Session OS13B-1733.

Stroup, J.B. and Fox, P.J., 1981. Geologic investigations in the Cayman Trough: Evidence for thin oceanic crust along the Mid-Cayman Rise. *J. Geology*, 89(4), 395-420.

Talwani, M., Worzel, J.L. and Landisman, M., 1959. Rapid gravity computations for two-dimensional bodies with application to the Mendocino submarine fracture zone. *J. geophys. Res*., 64, 49-59.

Taylor, B., Goodliffe, A. and Martinez, F., 2009. Initiation of transform faults at rifted continental margins. *Comptes Rendus Geoscience*, 341, 428-438, https://doi.org/10.1016/j.crte.2008.08.010.

ten Brink, U., Coleman, D. and Dillon, W.P., 2002. The nature of the crust under Cayman Trough from gravity. *Mar. Petrol. Geol.*, 19, 971-987.

Todd, B.J., Reid, I. and Keen, C., 1988. Crustal structure across the southwest. Newfoundland transform margin. *Can. J. Earth Sci*., 25, 744-759.

Tolstoy, M., Harding, A.J. and Orcutt, J.A., 1993. Crustal thickness on the Mid-Atlantic Ridge: Bull's-eye gravity anomalies and focused accretion. *Science*, *262*(5134), 726-729.

Van Avendonk, H.J.A., Hayman, N.W., Harding, J.L., Grevemeyer, I., Peirce, C. and Dannowski, A., 2017. Seismic structure and segmentation of the axial valley of the Mid-Cayman Spreading Centre. *Geochem. Geophys. Geosyst*., 18, 2149-2161.

Wessel, P. and Smith, W., 1998. New, improved version of Generic Mapping Tools released. *EOS, Trans. Am. geophys. Un.*, 79, 579.

White, R.S., 1979. Oceanic upper crustal structure from variable angle seismic reflection-refraction profiles. *Geophys. J. R. astr. Soc*., 57, 683-726.

White, R.S., 1984. Atlantic Ocean crust: seismic structure of a slow spreading ridge. In: Gass, I.G., Lippard, S.J. and Shelton, A.N. (eds.), Ophiolites and Oceanic Lithosphere, *Geol. Soc. Lond. Spec. Pub*., 13, 34-44.

White, R.S., Detrick, R.S., Sinha, M.C., et al. and Cormier, M.H., 1984. Anomalous seismic crustal structure of oceanic fracture zones. *Geophys. J. Royal ast. Soc*., 79(3), 779-798, https://doi.org/10.1111/j.1365-246X.1984.tb02868.x.

White, R.S., Mckenzie, D. and O'Nions, R.K., 1992. Oceanic crustal thickness from seismic measurements and rare earth element inversions. *J. geophys. Res*., 97, 683-715.

White, R.S., Minshull, T.A., Bickle, M.J. and Robinson, C.J., 2001. Melt generation at very-slow spreading oceanic ridge: constraints from geochemical and geophysical data. *J. Petrol*., 42, 6, 1171-1196.

Zelt, C.A., 1998. Lateral velocity resolution from three-dimensional seismic refraction data. *Geophys. J. Int*., 135, 1101-1112.

Zelt, C.A. and Barton, P.J., 1998. Three-dimensional seismic refraction tomography: a comparison of two methods applied to data from the Faeroe Basin. *J. geophys. Res*., 103, 7187-7210.

Zelt, C.A. and Ellis, R.M., 1988. Practical and efficient ray-tracing in two-dimensional media for rapid traveltime and amplitude forward modelling. *Can. J. Explor. Geophys*., 21, 16-31.

Zelt, C.A. and Smith, R.B.,1992. Seismic traveltime inversion for 2-D crustal velocity structure. *Geophys. J. Int*., 108, 16-34.

Zelt, C.A., Sain, K., Naumenko, J.V. and Sawyer, D.S., 2003. Assessment of crustal velocity models using seismic refraction and reflection tomography. *Geophys. J. Int*., 153, 609–626.

TABLES

Table 1. Summary of P-wave and S-wave inversion parameters (after Zelt and Barton, 1998).

Inversion parameter		***P-wave model***	***S-wave model***
sz		0.125	0.125
alpha		0.95	0.95
lambda0		100	100
lambda reduction factor		1.414	1.414
inversion cell – first phase	horizontal	2.0 km	3.0 km
	vertical	1.0 km	1.0 km
inversion cell – second phase	horizontal	1.0 km	1.0 km
	vertical	0.5 km	1.0 km

Table 2. Summary of *density model* block densities.

Crustal region	***Density kg m^{-3}***
continental crust	
upper	2600-2700
lower	2800-2950
mantle	3310-3315
oceanic crust	
upper	2500-2750
lower	2900-3060
mantle	3320-3340

Figures and captions on the following pages:

NOTE: The figures are low-resolution jpg versions of the original high-resolution postscript that would be used for production.

The low-resolution versions were created solely to achieve the upload file size restriction for submission for review.

FIGURES

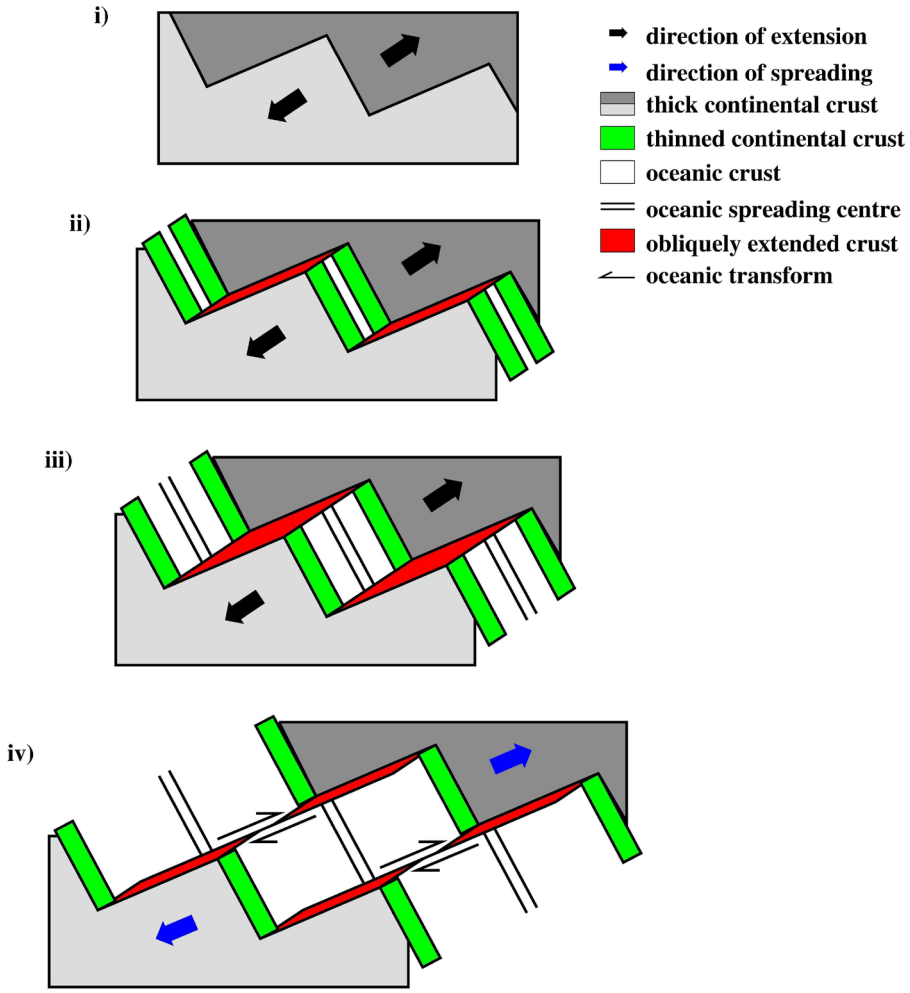

Figure 1. Conceptual model of transform margin evolution (Peirce et al., 1996; Greenroyd et al., 2007, after Mascle and Blarez, 1987; Mascle et al., 1997) through a series of stages comprising: (i) Stage 1 – rifting: initial intracontinental transform rifting; (ii) Stage 2 – drifting: continental crust thins in rift segments separated by transforms; and (iii) Stage 3 – aging: oceanic spreading results in the juxtaposition of old continental lithosphere against young oceanic lithosphere. iv) Eventually fossilization occurs as lateral motion across the fracture zone ceases. The Swan Islands margin is an example of a transform continental margin in the drifting (Stage 2) phase of evolution in a proximal mid-ocean ridge setting.

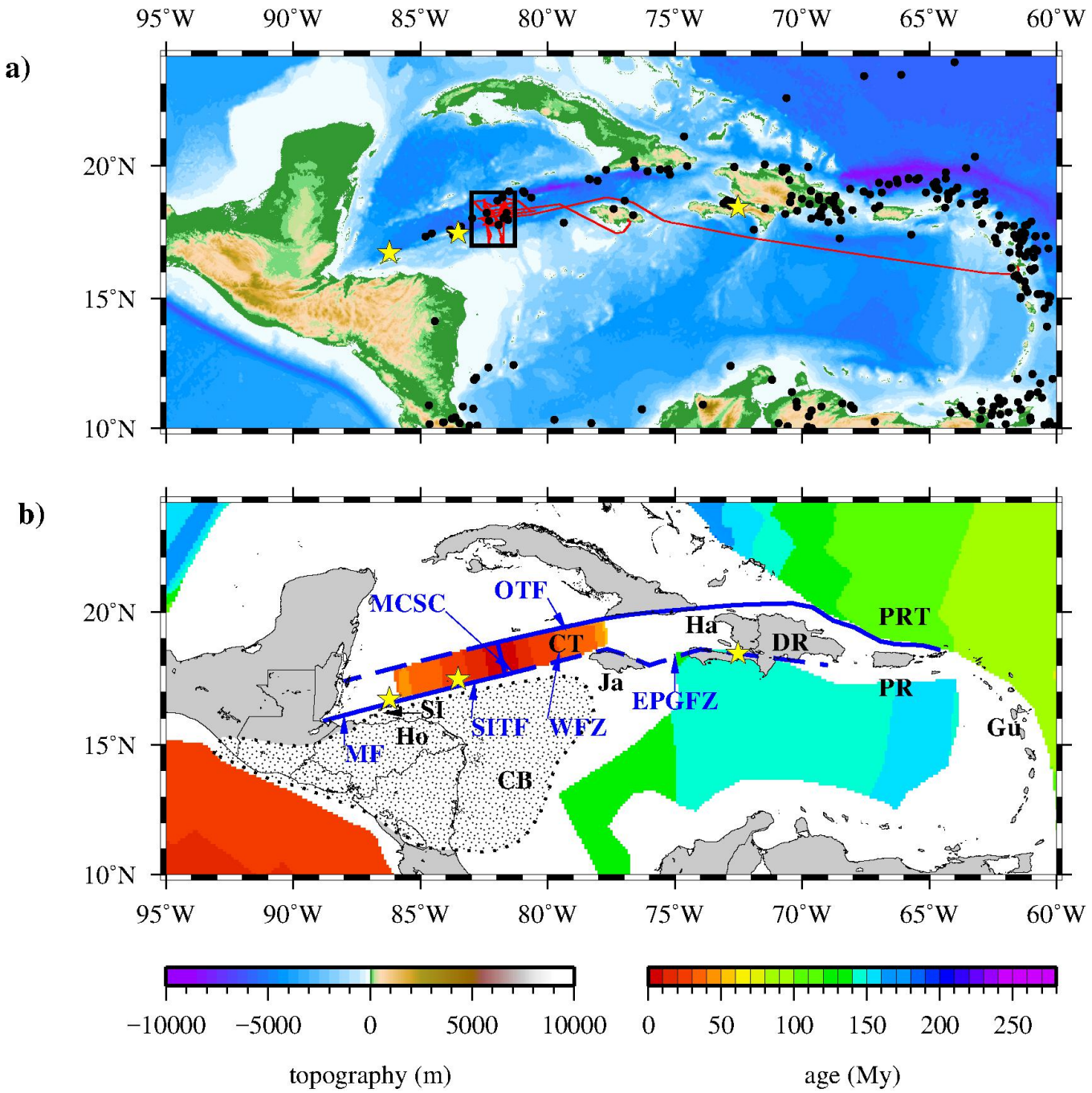

Figure 2. *CAYSEIS* project in the Cayman Trough. a) Port-to-port ship track (red line). Black dots show earthquake locations, with the yellow stars marking the 2009, 2010 and 2018 M_w >7 events (USGS Earthquake Hazards Program catalogue; https://earthquake.usgs.gov). Study area is outlined by the black box. b) Oceanic crustal age (after Müller et al., 2008) in the Cayman Trough (CT), with the Caribbean-North America plate boundary marked (blue line). Structural features: EPGFZ – Enriquillo-Plantain Garden Fault Zone; MF – Motagua Fault; MCSC – Mid-Cayman Spreading Centre; OTF – Oriente Transform Fault; WFZ – Walton Fracture Zone. Geographic features: CB – Chortis Block; DR – Dominican Republic; Gu – Guadeloupe; Ha – Haiti; Ho – Honduras; Ja – Jamaica; PR – Puerto Rico; PRT – Puerto Rico Trench; SI Swan Islands. Chortis Block is dotted (after Rogers et al., 2007a).

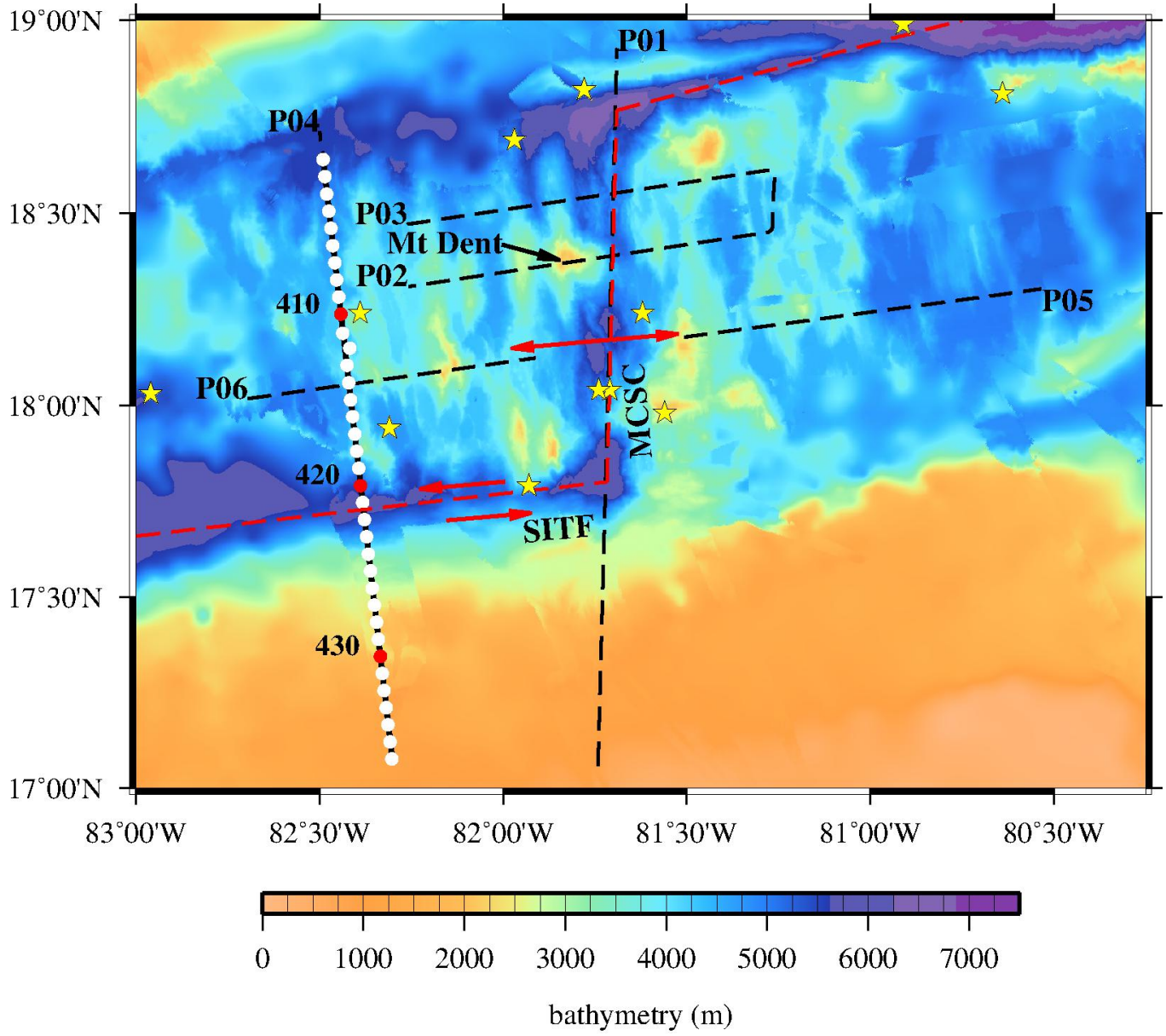

Figure 3. Cayman Trough and adjacent Honduran continental shelf and slope bathymetry. Profile P04 (solid black line) and OBSs (white dots) are marked. Red dots highlight OBS 410, OBS 420 and OBS 430 whose record sections are shown in Fig. 4. Dashed red line shows the Swan Islands Transform Fault (SITF) and the OTF, with red arrows showing its left-lateral slip direction and the spreading direction of the MCSC. Other profiles from the *CAYSEIS* experiment are shown by labelled black dashed lines. The Mt Dent OCC is labelled and earthquake epicentres are marked by yellow stars.

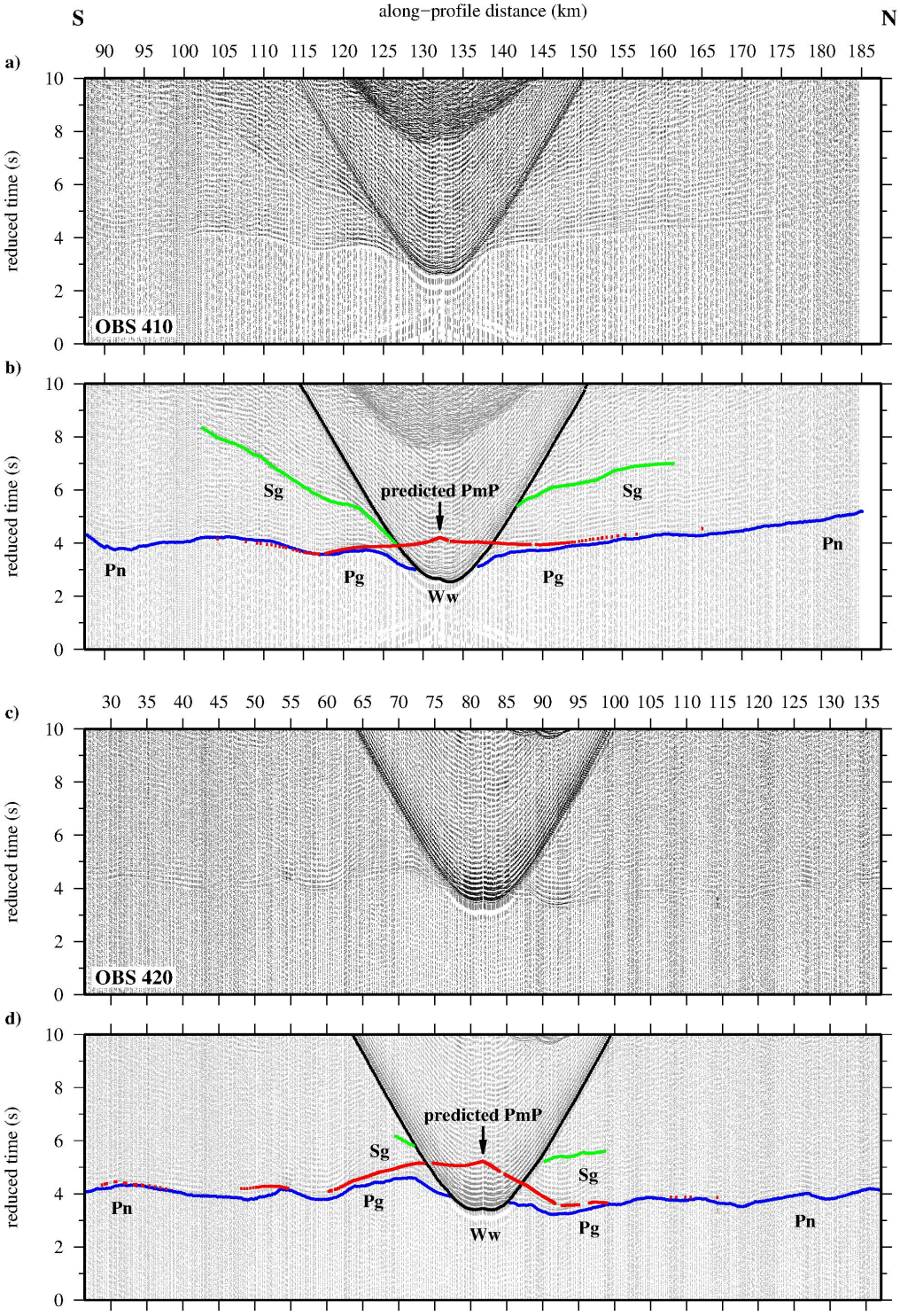
S
along−profile distance (km)
N
a)
b)
c)
d)
reduced time (s)
OBS 410
OBS 420
predicted PmP
Sg
Pn
Pg
Ww

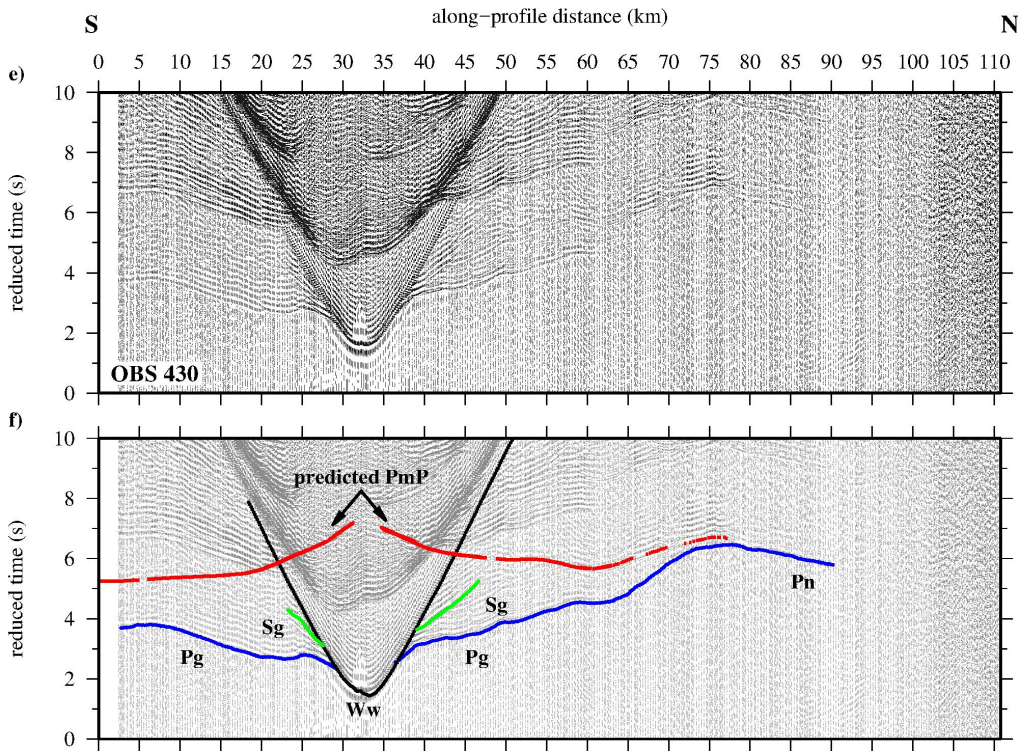

Figure 4. Example hydrophone WA refraction data sections (see Fig. 3 for location). a) Record section for OBS 410 plotted with a reduction velocity of 8 km s^{-1} and a 1-2-20-30 Hz band-pass filter. Horizontal axis shows along-profile distance (cf. Figs 5-9,11,13). b) Record section for OBS 410 showing observed water wave (Ww - black), crust and mantle P-wave (Pg and Pn - blue), and crustal S-wave (Sg - green) arrival travel time picks. Phases are labelled and travel time pick symbol size shows corresponding uncertainties. Predicted Moho reflection (PmP) based on forward modelling (Fig. 11) is also shown (red). c-d) Record sections for OBS 420. e-f) Record sections for OBS 430. Note: to the south of the SITF, PmP reflections are observed at ~55 to 80 km offsets on a number of OBSs.

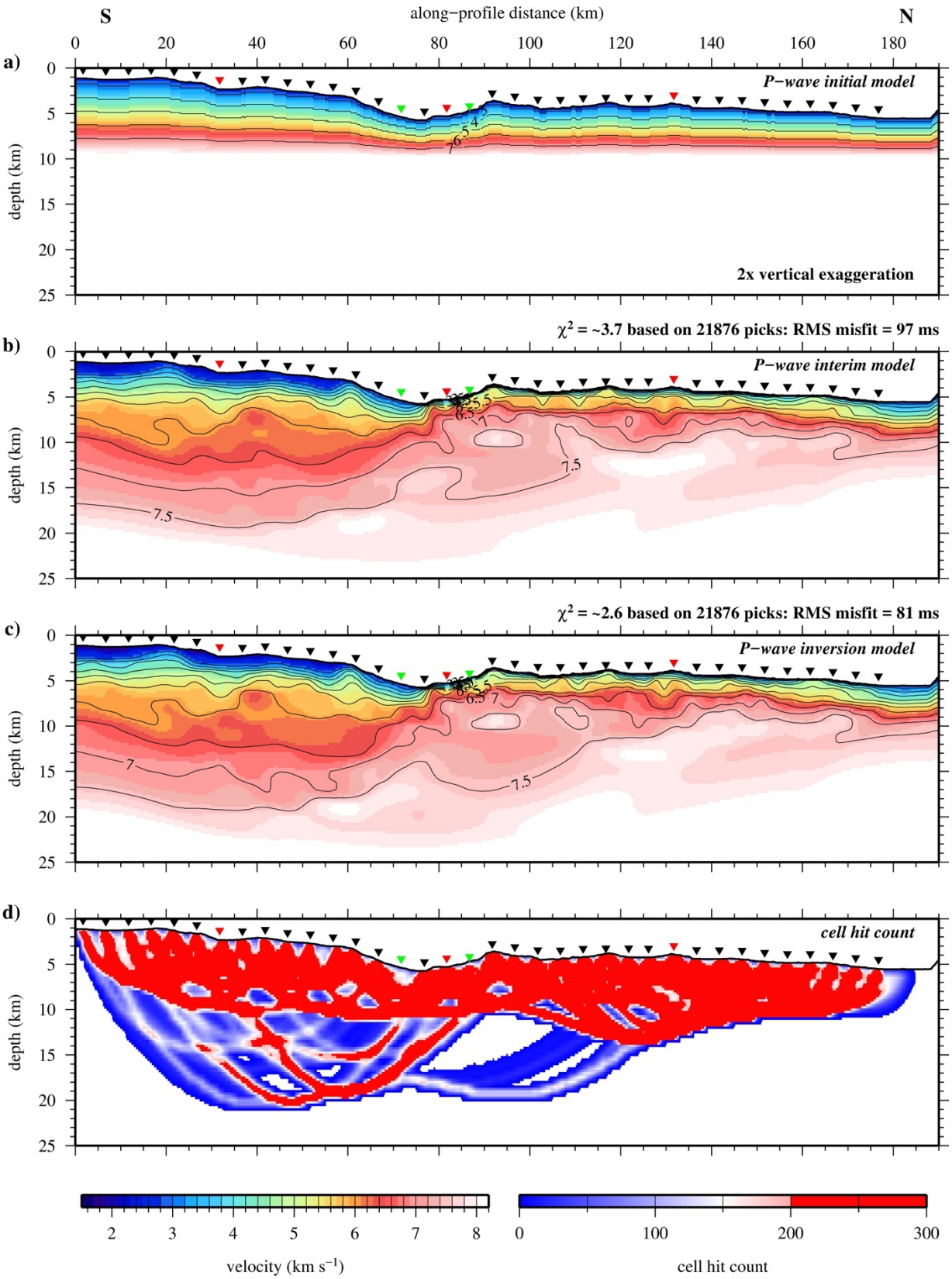

Figure 5. Inversion modelling. a) *P-wave initial model*. b) *P-wave interim model*. c) Best-fit *P-wave inversion model*. See text and Table 1 for approach and parameters adopted. χ^2 fit, the r.m.s. misfit (T_{RMS}) and the number of travel time picks are labelled for each stage. Velocity contours are plotted at 0.5 km s^{-1} intervals. d) Cell hit count indicatively showing ray coverage used to mask the *P-wave inversion model* in other figures. In all parts, OBS locations are marked by inverted black triangles, with OBSs 410, 420 and 430 highlighted in red, and OBSs 419 and 422 in green.

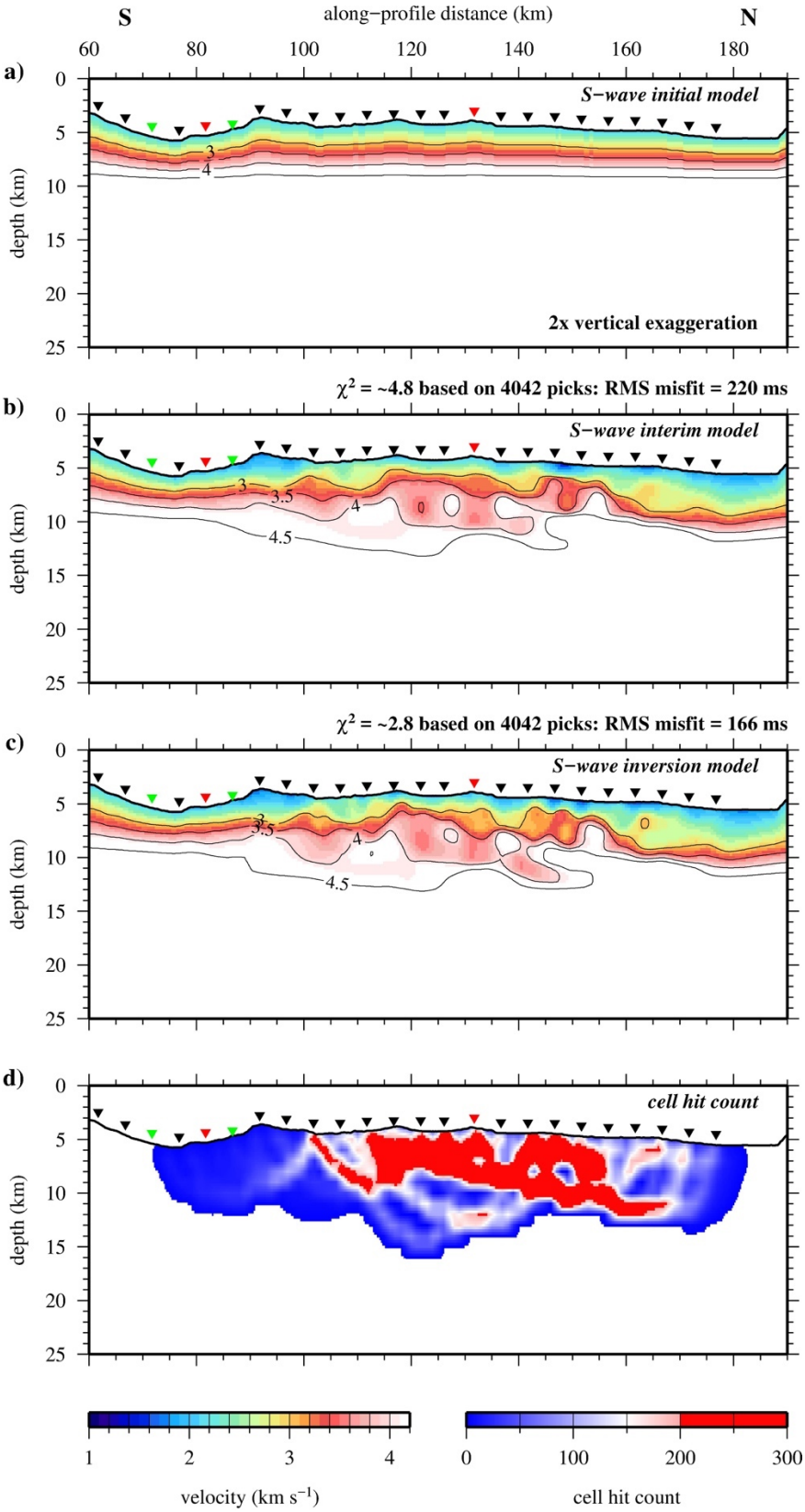

Figure 6. Inversion modelling. a) *S-wave initial model*. b) *S-wave interim model*. c) Best-fit *S-wave inversion model*. See text and Table 1 for approach and parameters adopted. χ^2 fit, the r.m.s. misfit (T_{RMS}) and the number of travel time picks are labelled for each stage. Velocity contours are plotted at 0.5 km s^{-1} intervals. d) Cell hit count indicatively showing ray coverage used to mask the *S-wave inversion model* in other figures. In all parts, OBS locations are marked by inverted black triangles, with OBSs 410, 420 and 430 highlighted in red, and OBSs 419 and 422 in green.

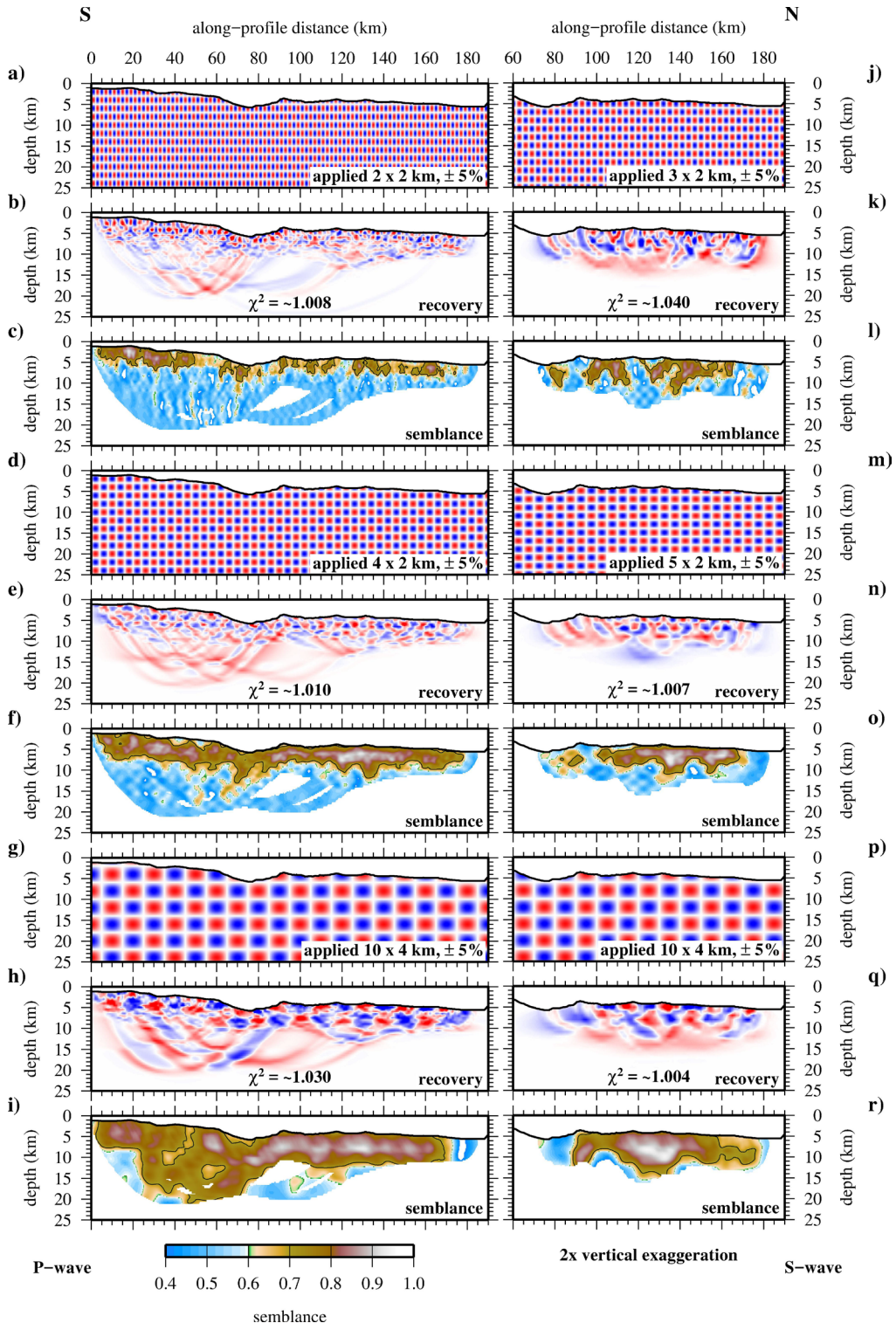

Figure 7. Checkerboard resolution testing of the *P-wave inversion model* (left) and *S-wave inversion model* (right). a) Checkerboard applied to the *P-wave inversion model* with a 2 x 2 km pattern size and 5% velocity anomaly. b) Recovered checkerboard. c) Semblance masked by ray coverage. A semblance of 0.7 is used as the good resolution threshold. χ^2 fit is annotated. A good resolution is achieved for the top 2-3 km of the crust. d-f) Checkerboard testing with a 4 x 2 km and 5% velocity anomaly checkerboard. A good resolution is achieved to ~5 km depth in the crust. g-i) Checkerboard testing with a 10 x 4 km and 5% velocity anomaly checkerboard. A good resolution is achieved to below Moho depth. j-l), m-o) and p-r) Equivalent checkerboard resolution testing of the *S-wave inversion model* with cell sizes as annotated.

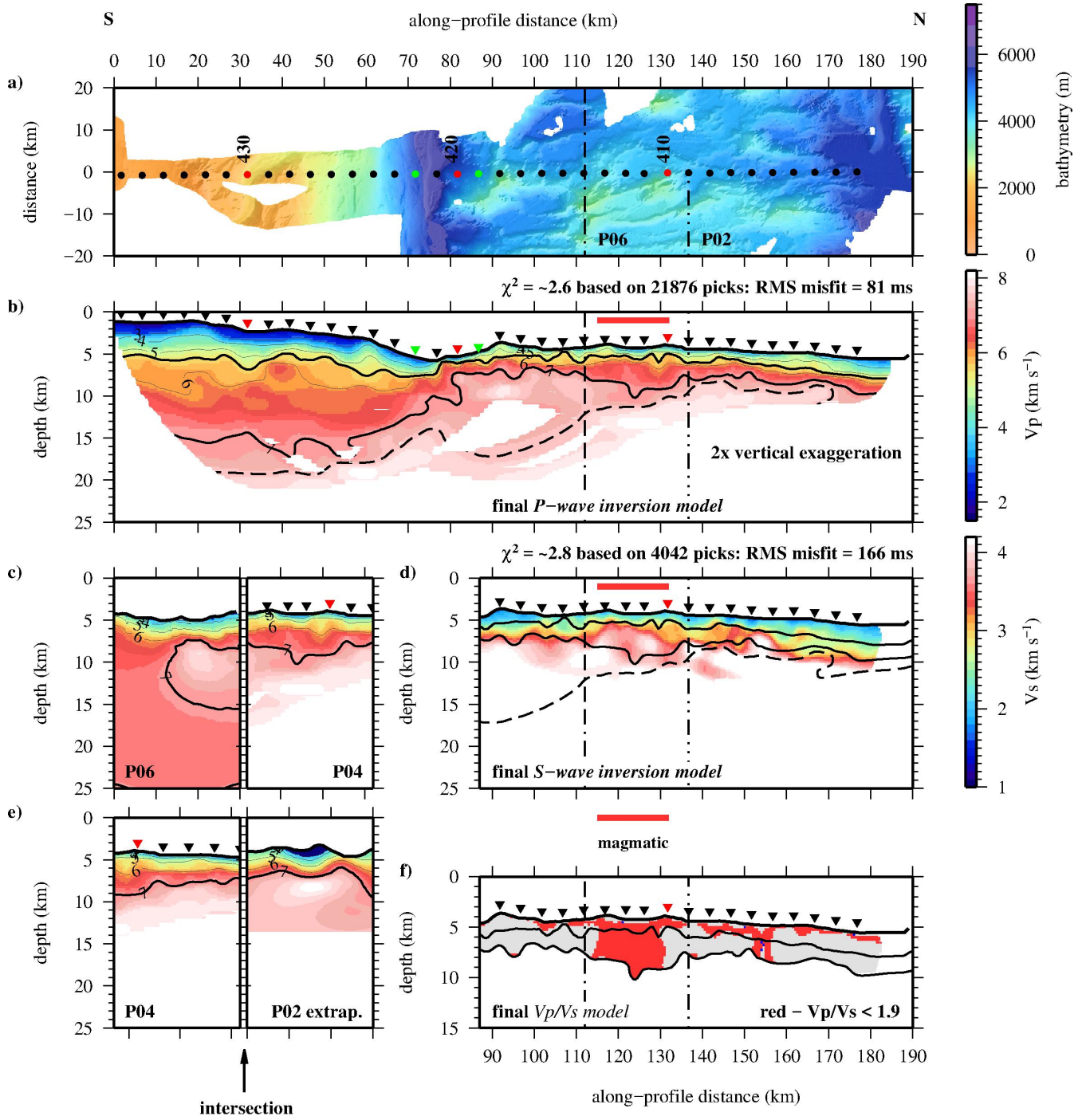

Figure 8. Comparison between *P-wave* and *S-wave inversion models*. a) Swath bathymetry. OBS locations (black dots/inverted triangles) shown in all parts, with OBSs 410, 420 and 430 (red dots/inverted triangles) and OBSs 419 and 422 (green dots/inverted triangles) highlighted. *CAYSEIS* Profiles P06 (intersecting) and P02 (extrapolated for 20 km beyond end of profile) are marked by dot-dashed lines. b) *P-wave inversion model* plotted with velocity contours at 1.0 km s^{-1} intervals. The 5.5 km s^{-1} contour marks the upper-to-lower crust transition, while the 7.0 km s^{-1} contour defines the Moho (black solid lines). The 7.5 km s^{-1} contour is also shown for reference (black dashed line). Solid red line marks the region of Profile P04 formed during a magma-rich phase at the ridge axis. c) Comparison between P-wave velocity-depth models for Profiles P06 and P04 at their intersection. d) *S-wave inversion model* with 5.5, 7.0, and 7.5 km s^{-1} P-wave velocity contours annotated. e) Comparison between P-wave velocity-depth models for Profiles P04 and P02 at their extrapolated intersection. f) *Vp/Vs model* showing crustal regions resulting from phases of magma-rich formation (<1.9 - red).

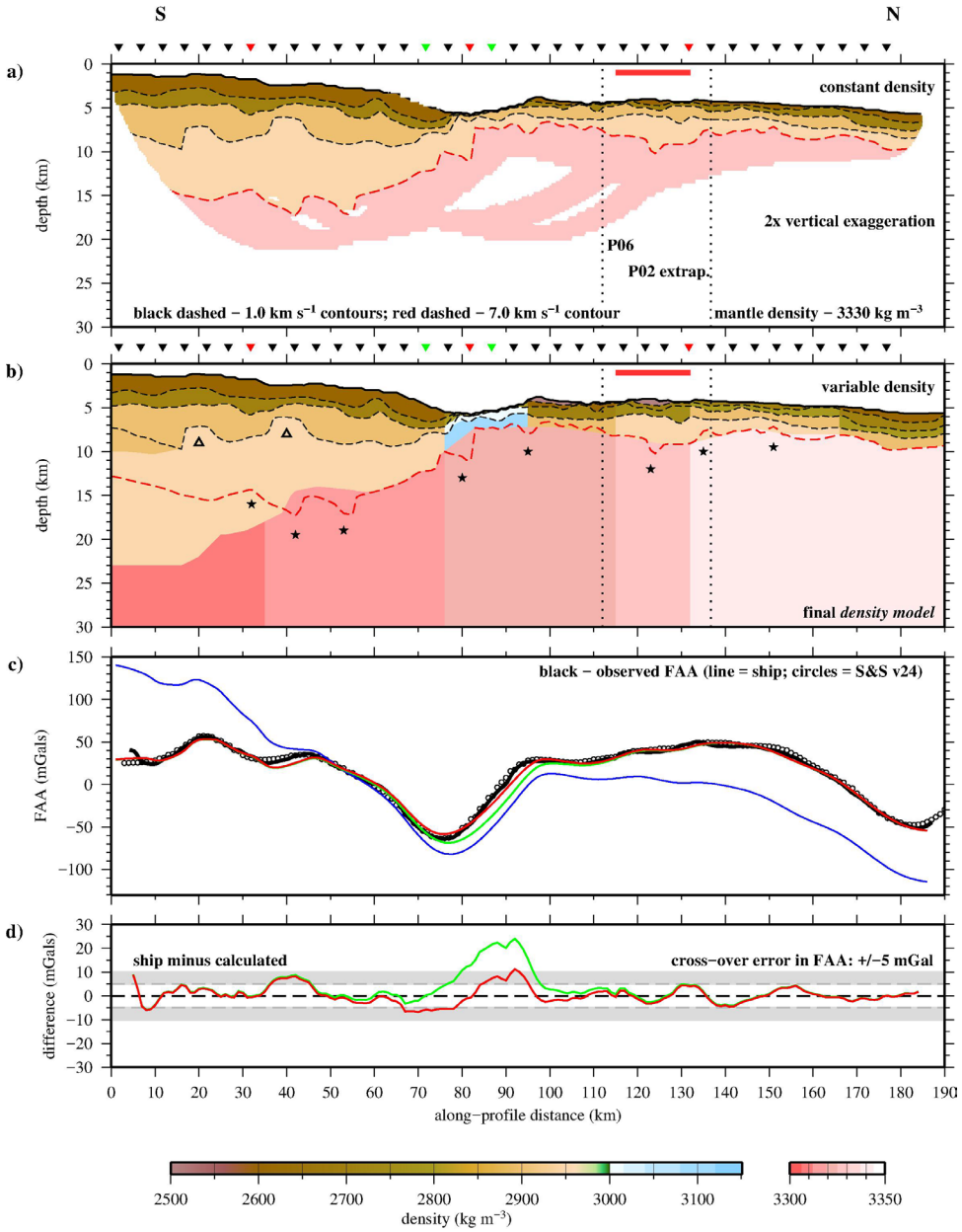

Figure 9. Gravity modelling test of the *P-wave inversion model*. a) Density-depth model with dashed lines marking the 4.0, 5.0 and 6.0 km s^{-1} (black) and 7.0 km s^{-1} (red) velocity contours used as block boundaries initially. Constant densities were applied to blocks within the same layer. Dotted vertical lines mark Profile P06 and P02 intersections, and the red line the region of Profile P04 formed during a magma-rich phase at the ridge axis. OBS locations are marked by inverted black triangles, with OBSs 410, 420 and 430 highlighted in red and OBSs 419 and 422 in green. b) *Density model* with variable densities within each layer, together with a gradation in density within the mantle, required to achieve the best-fit to the observed free-air anomaly (FAA). At the SITF (76 km to 95 km along-profile distance) higher densities are required throughout the crust. Open triangles mark regions interpreted as rifting-related basement topographic highs, while stars mark *P-wave inversion model* artefacts. c) Observed (ship – black line; Sandwell and Smith v24 – open circles) and calculated (coloured lines) FAAs, showing that higher density crust at the SITF is required to achieve a fit. Coloured lines represent anomalies calculated on the basis of: constant density blocks within layers (blue); variable density blocks within layers consistent with their continental or oceanic location (green); and variable density blocks required to achieve the best-fit (red). d) Misfit plotted against FAA error bounds.

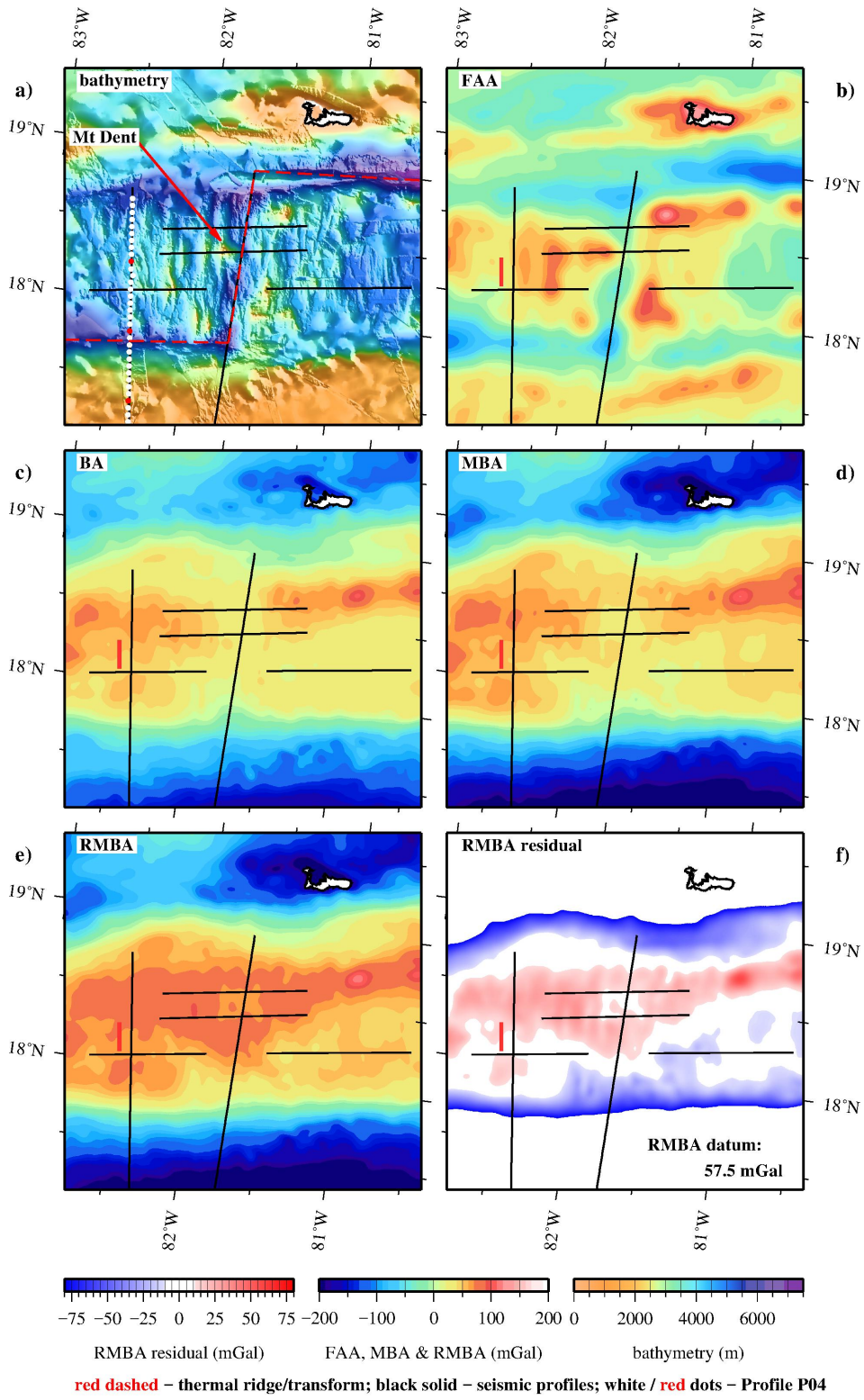

Figure 10. Residual mantle Bouguer anomaly for the MCSC and adjacent off-axis crust. a) Bathymetry with the locations of Profile P04 (solid black lines with OBSs as white and red circles) and other profiles (solid black lines) from *CAYSEIS* acquisition marked. Transform-ridge-transform geometry is marked by the dashed red line. b) Free-air anomaly (FAA) with solid red line marking the region of Profile P04 formed during a magma-rich phase at the ridge axis. c) Bouguer anomaly (BA). d) Mantle Bouguer anomaly (MBA). e) Residual mantle Bouguer anomaly (RMBA) calculated with the transform-ridge-transform geometry shown in a). f) RMBA residual showing areas of relative positive and negative anomaly. See text for discussion. The location of the Mt Dent OCC is highlighted.

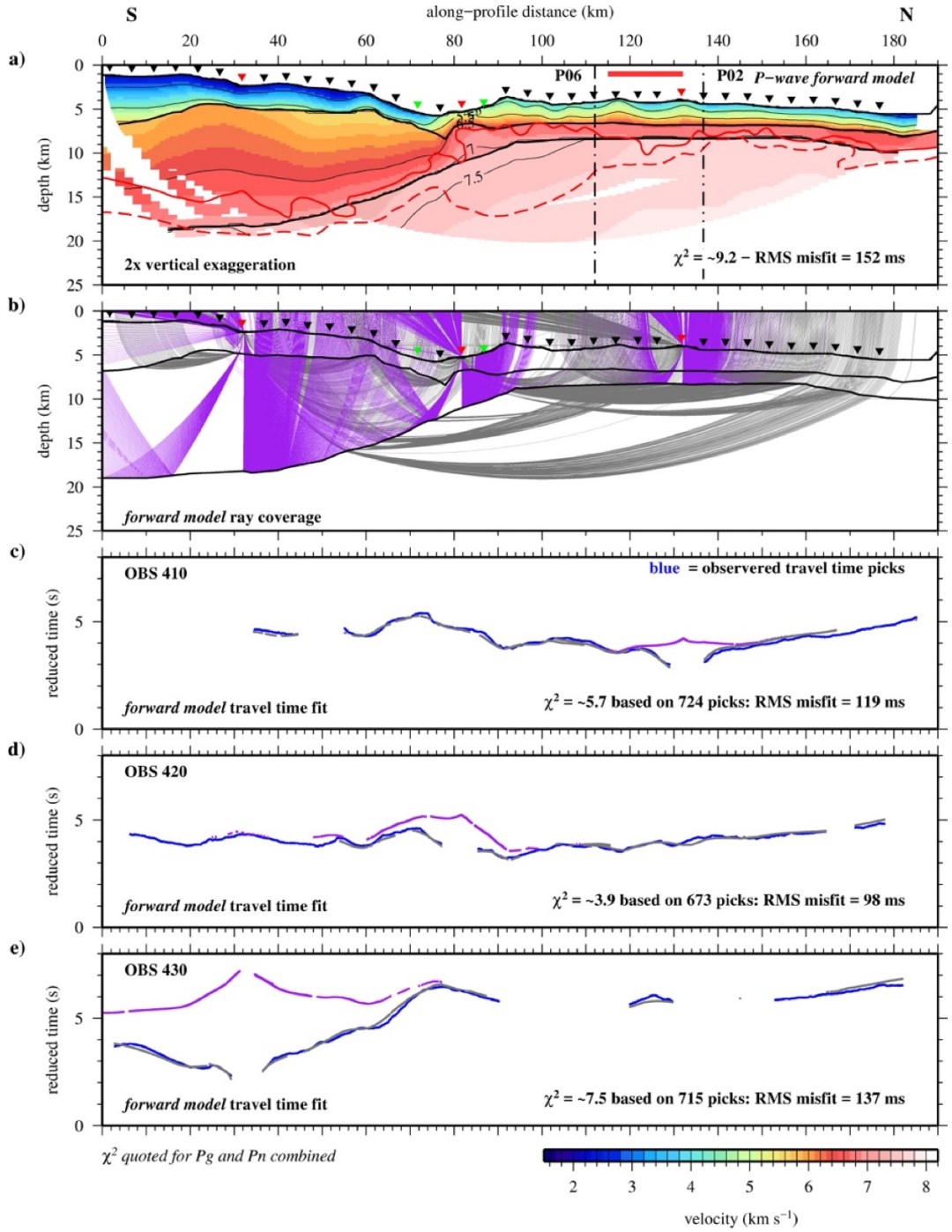

Figure 11. Forward ray-tracing to constrain the Moho. a) *Forward model* derived from the *P-wave inversion model* and using the 5.5 km s^{-1} contour to mark the boundary between the upper and lower crust. *P-wave inversion model* 7.0 and 7.5 km s^{-1} contours are shown for reference as solid and dashed red lines respectively. OBS locations are shown (black inverted triangles), with OBSs 410, 420 and 430 (red) and OBSs 419 and 422 (green) highlighted. *CAYSEIS* Profiles P06 (intersecting) and P02 (extrapolated for 20 km beyond end of profile) are marked by the dot-dashed lines. Solid red line shows the region of the modelled oceanic crust formed during a magma-rich phase at the ridge axis. b) Ray diagram for OBSs 410, 420 and 430, showing travel times point-to-point traced as both Pg and Pn phases (grey ray paths), and a predictive trace of where PmP arrivals (purple ray paths) should be observed. See text for discussion. c-e) Time-distance graphs for OBSs 410, 420 and 430 showing the ray traced arrivals (Pg and Pn – grey; PmP – purple) compared with observed arrivals (blue) with dot size set to pick error. The predicted PmP arrivals are shown on the corresponding data sections in Fig. 4.

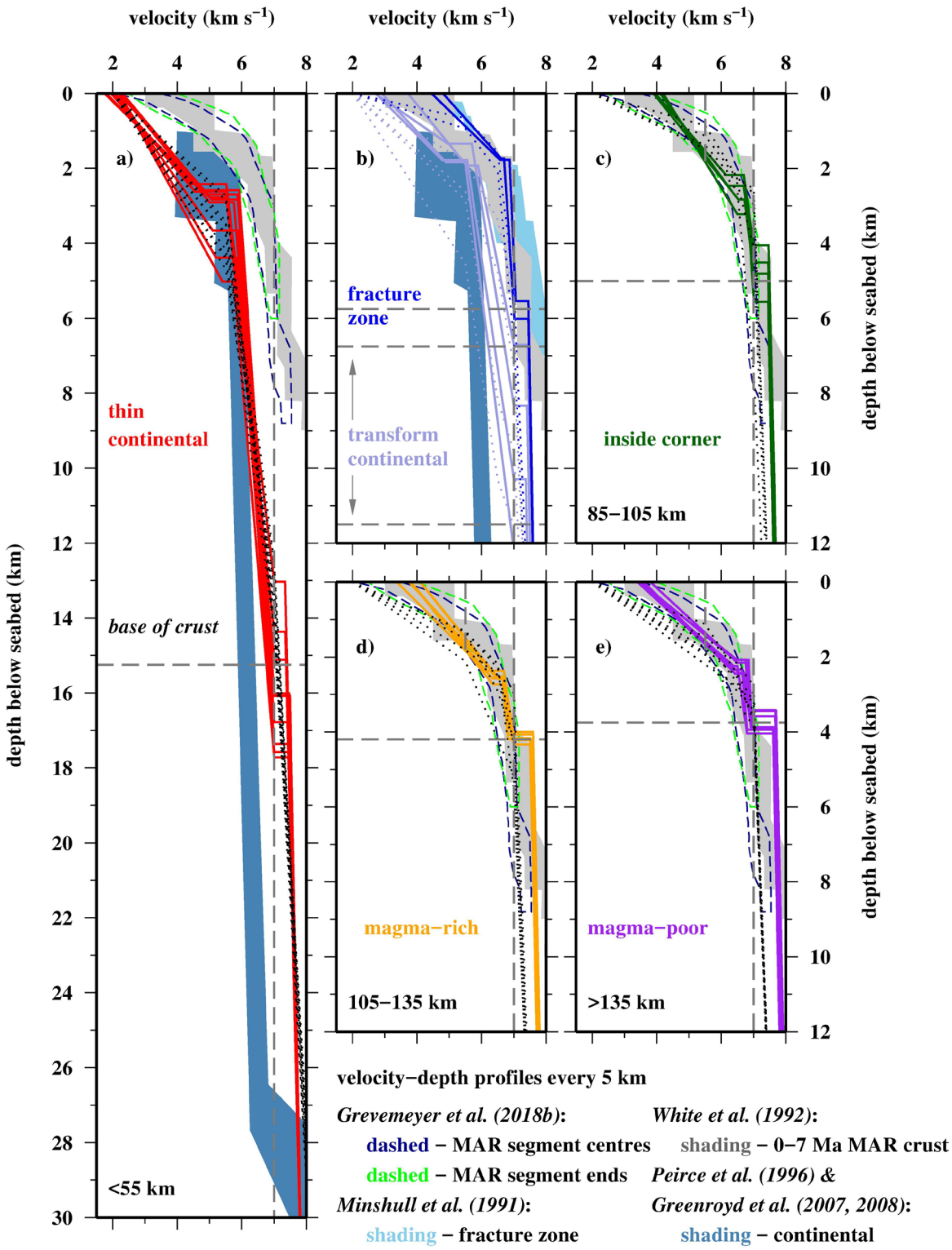

Figure 12. *P-wave forward* (solid lines) and *inversion* (dotted lines) *model* velocity-depth profiles. One-dimensional profiles, extracted at 5 km intervals, are colour-coded by setting along-profile: a) continental crust; b) transform continental and fracture zone crust; c) inside corner of the ridge-transform intersection; d) magma-rich; and e) magma-poor oceanic crustal formation. Average crustal thicknesses are marked (horizontal grey dashed lines). Profiles are compared to the Atlantic crustal velocity-depth envelopes of White et al. (1992) (grey shaded) and Grevemeyer et al. (2018b) (blue dashed = MAR segment centre crust; green dashed = MAR segment end crust), continental crustal (blue shaded) compilations of Peirce et al. (1996) and Greenroyd et al. (2007, 2008), and the fracture zone compilation (light blue shaded) of Minshull et al. (1991).

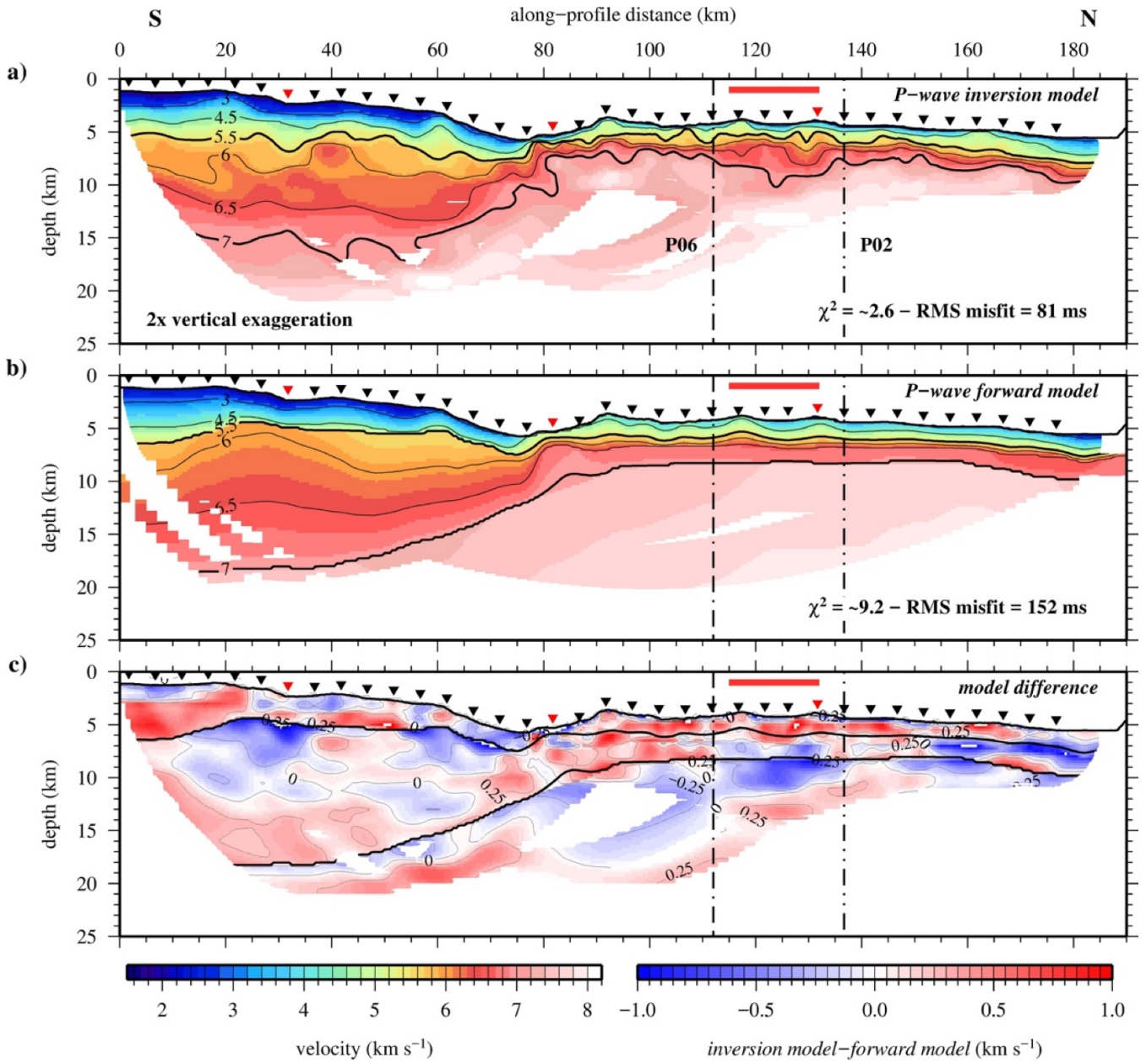

Figure 13. Comparison between P-wave velocity-depth models resulting from a) inversion and b) forward approaches to modelling. The 5.5 km s^{-1} velocity contour marks the transition from upper-to-lower crust and the 7.0 km s^{-1} contour denotes the Moho. OBS locations are shown (black inverted triangles), with OBSs 410, 420 and 430 (red) and OBSs 419 and 422 (green) highlighted. *CAYSEIS* Profiles P06 (intersecting) and P02 (extrapolated for 20 km beyond end of profile) are marked by the dot-dashed lines. Solid red line shows the region of the modelled oceanic crust formed during a magma-rich phase at the ridge axis. c) Calculated velocity difference between the two models, contoured at 0.25 km s^{-1} intervals. The inversion results in faster velocities in the upper crust than the forward ray-tracing approach. See text for discussion.